

1 **Mechanisms of ion selectivity and rotor coupling in the bacterial flagellar**
2 **sodium-driven stator unit**

3 Haidai Hu¹, Philipp F. Popp², Mònica Santiveri¹, Aritz Roa-Eguiara¹, Yumeng Yan¹, Zheyi Liu^{3,4},
4 Navish Wadhwa^{5,6}, Yong Wang^{3,4}, Marc Erhardt^{2,7}, Nicholas M. I. Taylor^{1,8*}

5 ¹Structural Biology of Molecular Machines Group, Protein Structure & Function Program, Novo
6 Nordisk Foundation Center for Protein Research, Faculty of Health and Medical Sciences,
7 University of Copenhagen, Blegdamsvej 3B, 2200 Copenhagen, Denmark.

8 ²Institut für Biologie/Bakterienphysiologie, Humboldt-Universität zu Berlin, Philippstr. 13, 10115
9 Berlin, Germany.

10 ³College of Life Sciences, Zhejiang University, Hangzhou 310027, China.

11 ⁴The Provincial International Science and Technology Cooperation Base on Engineering Biology,
12 International Campus of Zhejiang University, Haining, 314400, China.

13 ⁵Department of Physics, Arizona State University, Tempe, AZ, 85287, USA.

14 ⁶Biodesign Center for Mechanisms of Evolution, Arizona State University, Tempe, AZ, 85287,
15 USA.

16 ⁷Max Planck Unit for the Science of Pathogens, Berlin, Germany.

17 ⁸Lead contact

18 *Correspondence: nicholas.taylor@cpr.ku.dk

19

20 Abstract

21 Bacteria swim using a flagellar motor that is powered by stator units. These stator units are
22 energized by an ionic gradient across the membrane, typically proton or sodium. The presumed
23 monodirectional rotation of the stator units allows the bidirectional rotation of the flagellar motor.
24 However, how ion selectivity is attained, how ion transport triggers the directional rotation of the
25 stator unit, and how the stator unit is incorporated into the motor remain largely unclear. Here we
26 have determined by cryo-electron microscopy the structure of the Na⁺-driven type stator unit
27 PomAB from the gram-negative bacterium *Vibrio alginolyticus* in both lipidic and detergent
28 environments, at a resolution up to 2.5 Å. The structure is in a plugged, auto-inhibited state
29 consisting of five PomA subunits surrounding two PomB subunits. The electrostatic potential map
30 uncovers sodium ion binding sites within the transmembrane domain, which together with
31 functional experiments and explicit solvent molecular dynamics simulations, suggest a mechanism
32 for ion translocation and selectivity. Resolved conformational isomers of bulky hydrophobic
33 residues from PomA, in the vicinity of key determinant residues for sodium ion coupling of PomB,
34 prime PomA for clockwise rotation. The rotation is tightly blocked by the trans-mode organization
35 of the PomB plug motifs. The structure also reveals a conformationally dynamic helical motif at
36 the C-terminus of PomA, which we propose regulates the distance between PomA subunit
37 cytoplasmic domains and is involved in stator unit-rotor interaction, concomitant stator unit
38 activation, and torque transmission. Together, our studies provide mechanistic insight for
39 understanding flagellar stator unit ion selectivity and incorporation of the stator units into the
40 motor.

41 Introduction

42 Many bacteria rotate flagella to power their movement. The flagellum is characterized by a long
43 filament, connected through a flexible hook to cell envelope embedded rotary motor (or basal
44 body), which comprises a rotor and multiple stator units¹⁻⁴. The flagellar stator unit uses the
45 transmembrane ion motive force (IMF) to generate mechanical torque to rotate the flagellum,
46 which is employed by many bacteria to direct their locomotion in liquid environment or on viscous
47 surfaces to a favorable niche⁴⁻⁶. Driven by the stator unit, the bacterial flagellar motor can rotate
48 in both clockwise (CW) and counterclockwise (CCW) directions, with the switch between the two
49 directions controlled by intracellular chemotaxis signaling^{7,8}. The stator units are strictly required
50 for rotation of the flagellum and thus motility of the bacteria, but not for flagellar assembly^{9,10}. In
51 addition, the stator units dynamically associate with and dissociate from the rotor¹¹⁻¹³. Changing
52 the number of engaged stator units allows tuning the required torque in relation to the mechanical
53 load¹⁴⁻¹⁸.

54 Each stator unit is composed of two membrane proteins assembled as a complex buried inside the
55 cytoplasmic membrane, in which their transmembrane domains organize as an ion channel^{19,20}.
56 Incorporation of the stator unit requires its cytoplasmic domain to interact with the rotor and its
57 periplasmic domain to attach to the bacterial cell wall²¹. During activation, the stator unit
58 undergoes a conformational change from a plugged state into an unplugged one, and the
59 subsequent ion translocation through the stator unit drives its activity^{22,23}. Hence, the stator unit
60 itself is considered a "miniature" motor. Torque generated by ion translocation is transmitted to
61 the rotor via electrostatic interactions at the stator-rotor interface²⁴⁻²⁷. Depending on the
62 conducting ions, stator units can be grouped into two subfamilies: H⁺-driven stator unit (e.g.,
63 MotAB) and Na⁺-driven stator unit (e.g., PomAB)^{28,29}. In addition, stator units use potassium and
64 divalent ions such as calcium or magnesium as coupling ions have also been reported³⁰⁻³³.
65 However, at the molecular level, how stator units discriminate among different types of ions and
66 power rotation of the flagellar motor have remained unclear.

67 Recently, single particle cryo-electron microscopic (cryo-EM) structures of H⁺-driven MotAB
68 stator units^{34,35}, cryo-EM structures of intact flagellar motor complexes³⁶⁻³⁸, as well as *in situ* cryo-
69 electron tomographic (cryo-ET) studies of the flagellar motor^{21,39-41}, provided detailed structural
70 and functional views of stator unit assemble, torque generation and motor function¹. The data
71 strongly suggest a rotational model for the mechanism of action of the stator units. Upon dispersion
72 of the IMF, MotA is proposed to rotate around MotB, which is anchored to the peptidoglycan layer.
73 By engaging with the rotor MotA rotation powers the rotation of the large rotor. The differential
74 engagement of MotA with the rotor between the CW and CCW states of the rotor is proposed to
75 form the mechanistic basis of switching.

76 Cryo-EM reconstructions of the Na⁺-driven stator unit PomAB from *V. alginolyticus* (VaPomAB)
77 and *V. mimicus* have also been reported^{34,35}. However, due to the low resolution and anisotropic
78 maps, the atomic coordinates of the Na⁺-driven stator unit remain unknown. The Na⁺-driven stator
79 unit is particularly important for *Vibrio* species, including pathogenetic ones, as their polar flagella

80 can only be powered by the transmembrane Na⁺ gradient. Furthermore, the Na⁺-driven stator unit
81 is an ideal subject for investigating stator unit ion selectivity and translocation mechanisms. As a
82 Na⁺ ion interacts more with electrons than a proton in the cryo-electron microscope, it could
83 potentially be visualized more readily in a high-resolution cryo-EM map. Finally, sodium ions are
84 easier to be detected and manipulated than protons⁴².

85 The atomic structure of the Na⁺-driven stator unit is thus crucial for the mechanistic understanding
86 of how the stator unit distinguishes ions and couples ion transportation into its rotation. To this
87 end, we determined cryo-EM structures of *VaPomAB* in both detergent and lipidic environments,
88 with the local map resolution reaching up to ~2 Å. The high-resolution structure enabled us to
89 locate Na⁺ ion binding sites and revealed the structural and mechanistic basis of the ion selectivity.
90 We show at the molecular level how the stator unit achieves its monodirectional rotation upon ion
91 transport. Furthermore, we identified a helical motif C-terminal of PomA (CH) that is crucial for
92 stator unit function. We validated our structural results through extensive mutagenetic analysis and
93 molecular dynamics (MD) simulations. Finally, we propose a role for the asymmetric cytoplasmic
94 domain arrangement of the stator unit in the torque generation and the assembly and disassembly
95 mechanism of the stator unit into the motor.

96 Results

97 Structure determination and overall architecture of *VaPomAB*

98 Intact *VaPomAB* is an anisotropically shaped complex and shows preferential orientation of
99 particles in vitreous ice³⁵. To improve sample homogeneity, we modified the protein purification
100 protocol and encoded a protease site in the PomB gene after the plug region, which allowed for
101 the removal of the PomB peptidoglycan binding domain (PGB) during protein purification. To
102 overcome the preferred orientation, we added the zwitterionic detergent CHAPSO to randomize
103 particle orientation during EM grid preparation^{43,44}. Single-particle analysis yielded an overall
104 resolution of *VaPomAB* in LMNG detergent of approximately 2.5 Å resolution, with the cryo-EM
105 map of sufficient quality to build an atomic model for most of the protein complex. The local
106 resolution corresponding to the inner transmembrane domain approaches to 2 Å, with clear density
107 for non-protein molecules, allowing us to model water molecules and ions, as well as residue side
108 chains isomers (Fig. 1, Extended Data Fig. S2-S4 and Table S1).

109 PomAB assembles the characteristic bell shape of the stator unit family, with conserved 5:2 subunit
110 stoichiometry and overall architecture. Five PomA molecules arrange pseudo-symmetrically
111 around two PomB, with each PomA subunit comprising four transmembrane helices (TM1-TM4)
112 folded into two radial layers. The TM3s and TM4s form an inner layer lining the dimerized PomB
113 TMs. The TM1s and TM2s surround peripherally, together with PomA periplasmic interface (PI)
114 helices and cytoplasmic interface (CI) helices, establishing an outer layer, with one side packing
115 against the inner layer and the other side hydrophobically interacting with the lipid bilayer. The
116 resolved TM1 of one PomA makes prominent contact with the TM2 from the adjacent subunit.
117 The cytoplasmic domain of PomA contains a compact helix bundle (H1-H4), a region where torque
118 is generated through electrostatic matching with the rotor FliG torque helix⁴⁵. The cryo-EM map
119 of PomAB also reveals a short helix after PomA H4, which we designated as CH (C-terminal helix)
120 motif, attaching to the CI helix of a neighboring PomA subunit (Fig. 1f). The plugged motifs from
121 two PomB chains are fully resolved in our PomAB structure, where they are positioned on the top
122 of the periplasmic side of the stator unit, consistent with a plugged autoinhibited state. We also
123 noticed that each end of the plug motif interacts with the PI helix of PomA. We propose this causes
124 the N-terminal residues (residues 1–21) of two PomA subunits to be disordered, as these are not
125 resolved in our cryo-EM map (Extended Data Fig. S5c).

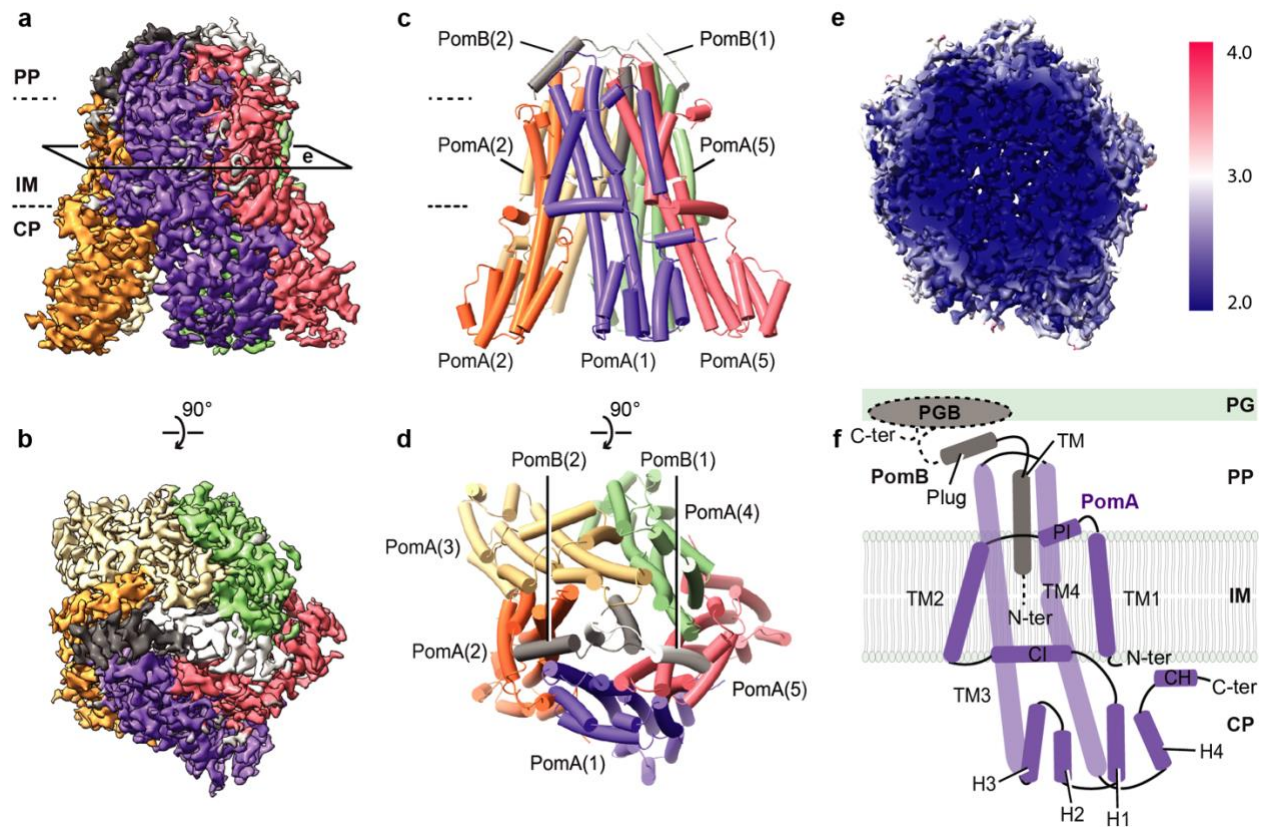


Fig. 1 Cryo-EM map and overall architecture of the Na⁺-driven stator unit VaPomAB.

a, Cryo-EM map of VaPomAB. PomA subunits (purple, orange, yellow, green and red) surround PomB subunits (black and white) viewed from the plane of the membrane. Dashed lines represent approximate inner membrane boundaries. **b**, Cryo-EM map of VaPomAB viewed from the periplasmic side. **c**, Ribbon model representation of VaPomAB. Subunits are colored as in **a**. **d**, VaPomAB model viewed from the periplasmic side. **e**, Local resolution map of VaPomAB viewed from a cross section as indicated in **a**. **f**, Topology diagram and secondary structural elements of VaPomA (purple) and VaPomB (black) subunits. The gray ellipse indicates the PomB peptidoglycan-binding domain (PGB). Abbreviations: PP, periplasm; IM, inner membrane; CP, cytoplasm; PG, peptidoglycan; TM, transmembrane; H, helix.

Plug motif and autoinhibition mechanism

The PomB plug motif is a short amphipathic α -helix, following the TM helix. Deletion of the plug motif results in ion influx into the cell cytosol, causing cell growth inhibition when overexpressed^{23,46}. Earlier studies through mutagenesis and cross-linking experiments have mapped critical residues involved in interactions between the PomB plug motif and PomA^{23,47}. In the PomAB structure, the TM of PomB is connected to the plug helix through a four-residue linker (Fig. 2c), which makes the plug helix turn approximately 145°, rendering its C-terminus to point towards the cytoplasmic membrane. The two short linkers establish interaction laterally by four backbone hydrogen bonds, organizing the plug motifs as a trans-mode configuration relative to

143 PomB TM helices, with a pseudo-mirror symmetry perpendicular to the cell membrane (Fig. 2a,
144 2d). The plug motifs from sodium and proton- driven stator units share a similar amino acid pattern
145 (Extended Data Fig. S1b) comprising a hydrophobic side that makes its main interaction with the
146 stator unit itself and a hydrophilic side that is exposed in most parts to the periplasmic space solvent
147 (Fig. 2b). The contact environment of the PomB plug motif is mainly contributed by a cleft framed
148 by the periplasmic side of the TM4, TM3 and the PI helix from one PomA subunit, and the
149 periplasmic side of the TM3 and TM4 from the adjacent PomA subunit. Three residues from the
150 plug motif (I50, M54 and F58) deeply insert into this cleft, establishing hydrophobic interactions
151 (Fig. 2e-f). Additionally, the PomB F47 aromatic ring is sandwiched between the pyrrolidine ring
152 of P172 and the side chain of M169 from PomA, via CH- π interactions, further stabilizing the plug
153 motif (Fig. 2f). The 5:2 stoichiometry of the stator unit creates inequivalent binding environments
154 for the two plug motifs, as examined by calculating the surface buried area and free energies of
155 residues forming the plug helix (residues 44-58, Fig. 2g-h). Therefore, we speculate that during
156 stator unit activation, releasing the plug motif from the stator unit is not a symmetric process.
157 Instead, one plug motif with relatively low binding energy likely detaches from its inhibitory site
158 first, and the second plug motif will then be induced to be released. PomB G59 marks the end of
159 the plug motif, and it directly exerts the effect on the conformation of PomA PI helix. We found
160 that each of the PomB plug motifs induces two different conformations of the PomA PI helix that
161 links PomA TM1 and TM2; one conformation is akin to those observed in the other three PomA
162 subunits, and the other conformation extends TM2 one more helical turn involving residues from
163 L26 to V32 (Extended Data Fig. S5c).

164 The dynamics of the PomA PI helices stemming from the PomB plug motif interaction presumably
165 drives the flexibility of the corresponding TM1, as the latter could not be resolved in two of the
166 PomA subunits. The high-resolution PomAB structure was determined in a detergent micelle
167 environment, raising the possibility that detergent molecules could have an impact on the
168 conformation of PomAB, particularly the membrane-facing helices, including the disordered TM1
169 from two PomA subunits. To clarify this and to better mimic the native environment of the stator
170 unit, we reconstituted *Va*PomAB into membrane scaffold protein 1D1 (MSP1D1) nanodiscs, as
171 well as full length, non-cleaved *Va*PomAB into saposin nanodiscs, with *E. coli* polar lipids, and
172 determined the map resolution, at 3.9 Å and 6.3 Å, respectively (Extended Data Fig. S3-S4). In
173 both cases, we were able to trace all the secondary structure elements of the PomAB complex,
174 except those two PomA TM1 helices (Extended Data Fig. S5f, S5i). Comparison of the PomAB
175 LMNG structure to the MSP1D1 lipid-reconstituted structure did not reveal major conformational
176 differences (root-mean-square deviation of 0.36 Å) that could arise from detergent artifacts. This
177 indicates that the flexibility of those two TM1 helices in the inactive stator unit is probably intrinsic,
178 which might be functionally important during stator unit activation.

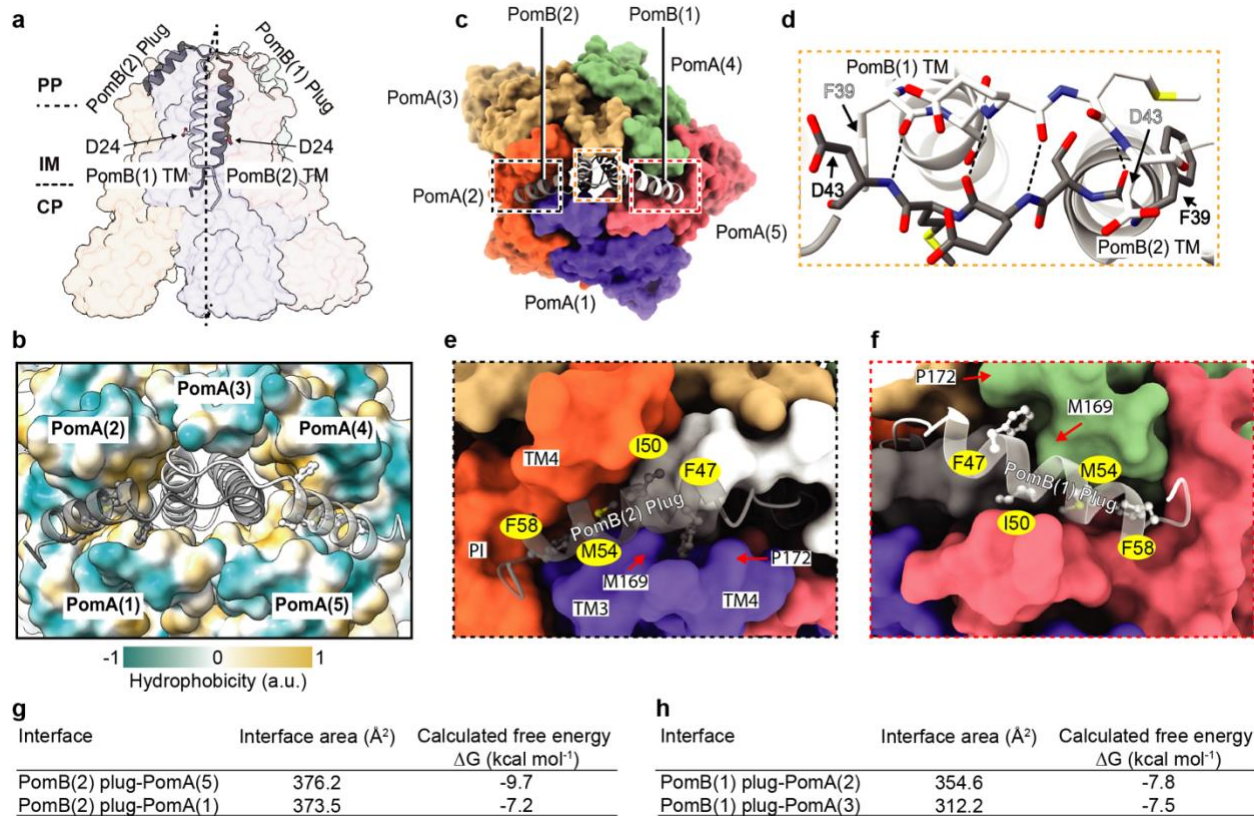


Fig. 2 PomB plug motif and auto-inhibition mechanism.

a, *VaPomAB* in its auto-inhibited state, viewed from the plane of the membrane, with PomB shown as ribbons (black and white) and PomA shown as a semitransparent surface representation. The aspartate residues D24 from both PomB TM are indicated and shown as sticks. **b**, Top view of *VaPomAB* with PomB shown as ribbons and PomA shown as a surface representation colored according to its hydrophobicity. **c**, Top view of *VaPomAB*. PomA subunits are shown as a surface representation and PomB subunits are displayed as ribbons, colored as in Fig. 1a. **d**, Close-up view from the periplasmic side of the interactions of the linkers (Phe39-Asp43) that connect PomB plug motifs and TMs (it corresponds to the yellow box in **c**). Hydrogen bonds are represented as dashed lines. **e**, Plug motif from PomB(2) binding environment (black box in **c**). **f**, Plug motif from PomB(1) binding environment (red box in **c**). **g-h**, Calculated interface buried area and free energy of PomB plug motifs.

Na⁺ ion binding sites and ion selectivity mechanism

Stator units use specific ions to power the flagellar motor rotation. Each MotB/PomB TM contains an aspartate (D24 in PomB) that is responsible for the binding and translocation of incoming ions from the periplasmic space to the cytoplasmic side (Fig. 2a). However, this aspartate is universally conserved among stator unit families (Extended Data Fig. S1b), obscuring the structural and mechanistic basis of the ion selectivity. The PomAB structure shows that D24 from two PomB chains sit in a different environment; D24 of Pom B chain 1 interacts with PomA, which we refer to as an engaged state; while D24 of PomB chain 2 points towards the cytoplasmic domain and

196 breaks the interaction with PomA, which we refer to as a disengaged state (Fig. 3a). Examination
197 of the high-resolution density map in the vicinities of these two aspartates reveals nonresidue
198 densities. In site 1, close to the engaged PomB D24 (PomB chain1), the extra density is coordinated
199 by oxygens from side chain hydroxyl groups of PomB T21 and D24, and backbone carbonyl
200 groups of adjacent PomA P151 and PomB G20. A fifth coordinating interaction is made by a
201 hydrogen bond from a water molecule near PomA A190, with the average distance between the
202 center of the density and associated oxygens is 2.88 Å (Fig. 3b). In site 2, near the disengaged
203 PomB D24, which is more flexible as indicated by the slightly blurred EM density of its acidic
204 side chain, a globular density is well coordinated by oxygen atoms exclusively contributed by
205 PomA TM3 and TM4: side chain hydroxyl groups of T158, T185 and T186, and exposed backbone
206 carbonyl groups of G154 and A182, with an average distance between the density center and
207 associated oxygen of 2.33 Å (Fig. 3c). Given the cation's favorable local chemical environments
208 in these two sites, and especially the typical geometry of Na⁺ coordination⁴⁸ in site 2, we modeled
209 these densities as Na⁺ ions, which were the most predominant cations in the protein purification
210 buffer. To further validate the model, we performed two explicit solvent all-atom MD simulations
211 (1 μs for each) and observed that the Na⁺ ion in site 1 was very stable, but the other Na⁺ ion in site
212 2 rapidly moved to an intermediate site formed by the side chain of D24, T158 and T186 and
213 subsequently to a location symmetric to site 1, and finally released to the cytoplasmic space
214 (Extended Data Fig. S6c-d and Supplementary Movie 1). We also observed significant
215 conformational dynamics of a few polar residues around site 2, especially T158, T186 in PomA
216 chain 5 and D24 in PomB chain 2 (Extended Data Fig. S6a and S7). By contrast, T186 in PomA
217 chain 2 and D24 in PomB chain 1 on the engaged site were however much more stable (Extended
218 Data Fig. S6a-b and S7d).

219 The identification of the Na⁺ binding sites from EM density and the asymmetric conformational
220 dynamics led us to speculate that at least part of the PomAB ion selectivity filter nests within the
221 PomA subunit, and those three threonine residues (PomA T158, T185 and T186), which are
222 conserved in all sodium-driven stator units (Extended Data Fig. S1a), account for the Na⁺ ion
223 selectivity and transportation. Of note, the T158 from PomA chain 2, near the engaged PomB D24,
224 does not directly contribute to the Na⁺ binding. Instead, it orients its side chain to establish a
225 hydrogen bond with PomB D24 (Fig. 3b), indicating that a local conformational change occurs
226 during Na⁺ ion transportation. Similarly, on the same site of the other three PomA subunits, we
227 did not observe densities corresponding to a Na⁺ ion (Extended Data Fig. S8a-f), suggesting only
228 one Na⁺ ion would be supplied during stator unit rotational steps.

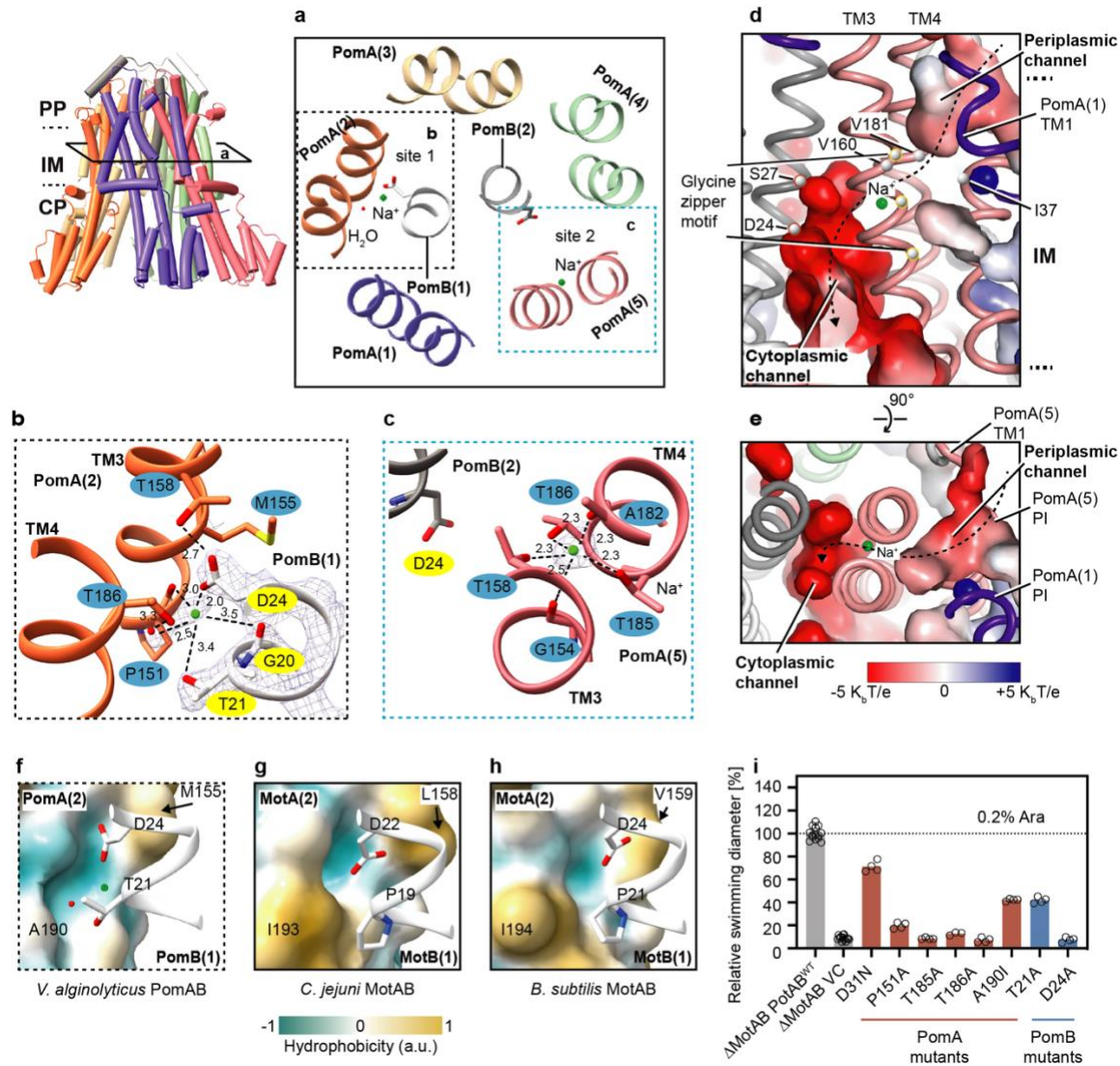


Fig. 3 Ion binding sites, selectivity, and translocation pathway.

a, Cross section view (corresponding to the view in left panel and rotated 90°) of Na⁺ ion binding sites (cyan spheres) in the vicinities of the two Asp24 from PomB. **b**, Details of the Na⁺ ion binding site near PomB(1) engaged Asp24. For clarity, corresponding EM densities are only overlapped in the region of PomB(1) Gly20-Asp24, Na⁺ ion, and water molecule. Hydrogen bonds are indicated as dashed lines with distances in angstroms. **c**, Details of the Na⁺ ion binding site near disengaged PomB(2) Asp24. EM density is overlaid on the Na⁺ ion. **d**, Na⁺ ion translocation pathway (dashed line with arrow). Periplasmic and cytoplasmic channels are indicated, with surface colored by electrostatic potential (positively charged, blue; negatively charged, red). Ca atoms of the residues forming the putative hydrophobic gate, of the glycines forming the glycine zipper motif, and of the PomB (2) S27 and D24 Ca are indicated and shown as spheres **e**, Top view of the Na⁺ ion translocation pathway. **f**, *Va*PomAB sodium ion binding environment near the engaged site. The surface of PomA is colored by hydrophobicity. **g**, Similar view as in **f**, but in the proton-driven stator unit *Cj*MotAB. **h**, Similar view as in **f**, but in the proton-driven stator unit *Bs*MotAB. **i**, Comparison of motility ability of the *Va*PotAB constructs and point mutants of the residues near the Na⁺ ion binding site or residues along Na⁺ translocation pathway.

229
230
231
232
233
234
235
236
237
238
239

240 To probe the critical role of key residues for the functional ion selectivity of Na⁺-driven stator unit,
241 we first designed a chimeric PomAB (renamed as VaPotAB) by replacing PomB PGB with *S.*
242 *enterica* MotB PGB, a strategy similar to that used in previous studies^{49,50}. A plasmid encoding
243 VaPotAB conferred a motile phenotype on soft agar plates when transformed into a mutant
244 *Salmonella enterica* strain that lacks MotAB (Fig. 3i). We then made point mutations based on
245 VaPotAB to evaluate the significance of the three key threonines on flagellar motor rotation by
246 examining the motility phenotype. We found that substituting any of these three threonines to
247 alanines abolishes bacterial motility, confirming the importance of these residues to stator unit
248 function. The Na⁺ ion binding cavity therefore seems a strict requirement for ion selectivity. A K⁺
249 ion, which has a larger radius than Na⁺ ion (1.52 Å vs 1.16 Å) and has an average ligated bond
250 distance of around 2.7-3.2 Å, cannot be accommodated in this cavity. On the other hand, H⁺ is too
251 small to fill this cavity, and it is energy unfavorable for a H₃O⁺ to be ligated with a coordination
252 number of five. Therefore, K⁺ and H⁺ (or H₃O⁺) cannot be used by PomAB as coupling ions.
253 Divalent ions, such as Ca²⁺ and Mg²⁺, which would need further negatively charged residues to be
254 neutralized and coordinated, are therefore not favored in this cavity either.

255 Additionally, we compared the PomAB structure with the available H⁺-driven stator unit structures,
256 *C. jejuni* MotAB and *B. subtilis* MotAB, to explore the reason why H⁺-driven stator units cannot
257 use sodium or other alkaline metals as coupling ions. In the part of the structure of the H⁺-driven
258 stator unit that is equivalent to the corresponding Na⁺ binding site 2 in PomAB, two threonines
259 (T158 and T185) are replaced by alanine, lacking oxygen in this cavity, likely precluding alkaline
260 metal ion binding (Extended Data Fig. S1a). In the equivalent position of the PomB engaged D24,
261 near the water molecule that coordinates the Na⁺ binding site 1, the H⁺-driven stator unit contains
262 an isoleucine residue instead of an alanine or a polar residue, which makes this region hydrophobic
263 and does not favor an alkaline metal ion coordination (Fig. 3f-h). Thus, both sites in the H⁺-driven
264 stator unit lack the contact environment for alkaline metal ions, and these analyses further support
265 the idea that the residue variability in PomA/MotA has a large influence on ion selectivity.

266 Analysis of the structure assembly interface between PomA and PomB subunits at the periplasmic
267 level reveals that this inner contact interface is mainly lined by hydrophobic residues (Fig. 4a),
268 with the thickness spanning around four helical turns (from PomB S27 to S38). It is therefore
269 unlikely that an aqueous channel that mediates the Na⁺ ion flow through PomAB is formed in this
270 region. Rather, a potential Na⁺ translocation pathway could be delineated based on the PomAB
271 structure and our functional motility assay. It extends from the Na⁺ binding site 2 to the periplasmic
272 space, delineated on one side by the PI helix and the beginning of TM2 helix from the same PomA
273 subunit and on the other side by the end of TM1 from the adjacent PomA subunit (Fig. 3d-e). The
274 ion translocation pathway in this part contains a hydrophobic gate (Fig. 3d), likely removing the
275 hydration shell of the incoming Na⁺; and towards the periplasmic space, the translocation pathway
276 is lined by several polar residues, such as D31, T33 and S34, and many of them are conserved
277 (Extended Data Fig. S9b-c). The Na⁺ translocation pathway reaches to the PomB D24 and to PomA
278 cytoplasmic domain inner lumen, where the surface electrostatic potential is very negative (Fig.
279 4d), and, together with the N-terminus of PomB that harbors several negatively charged residues

280 (Extended Data Fig. S1b), might attract the incoming Na⁺. We also found that PomA TM3 contains
281 a strictly conserved GXXGXXXG (residues G154-G161) motif, a typical ‘glycine zipper’
282 structure contributing to channel formation in many membrane proteins⁵¹. Glycines from the
283 ‘glycine zipper’ motif face TM3 and TM4 assemble interface, holding the Na⁺ selectivity filter in
284 a middle position, and together with the conserved P151, contributing to the main chain
285 conformational elasticity of this region when a Na⁺ ion passes through TM3 and TM4 cleft (Fig.
286 3d, Extended Data Fig. S1a and S9c).

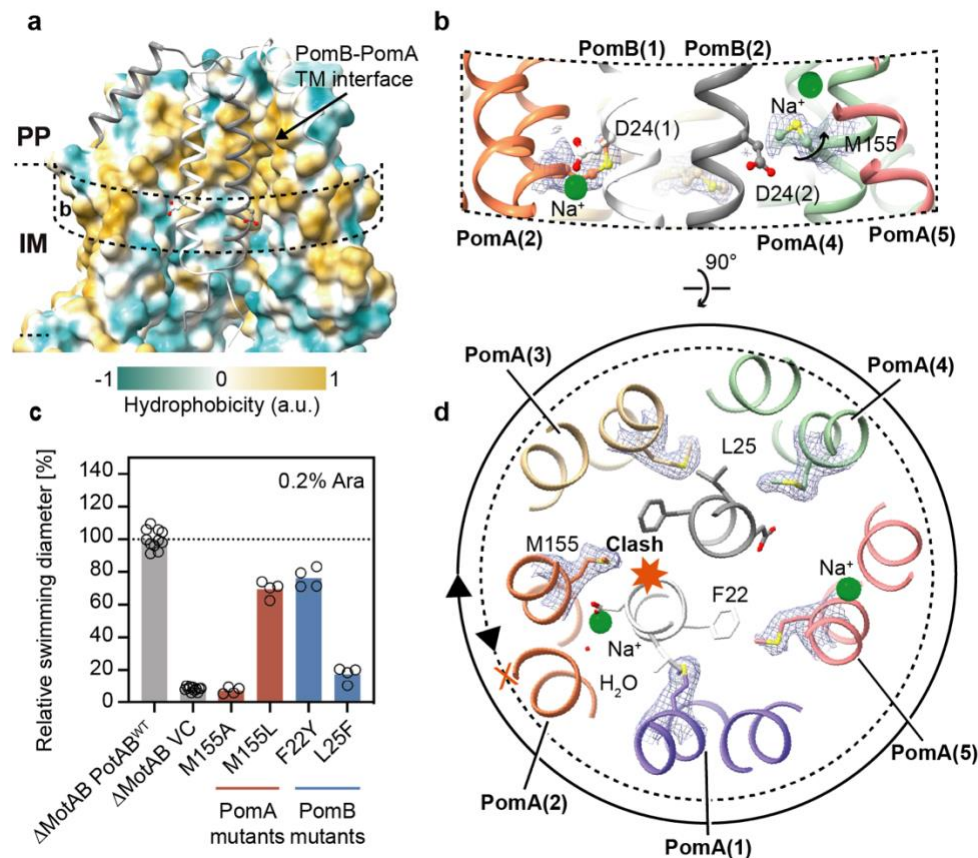
287 From our explicit solvent MD simulations, we also observed that in the periplasmic side, the side
288 chain of T33 was conformationally dynamic and surrounded by water molecules, which could
289 occasionally diffuse to the space next to the side chain of T185 (Extended Data Fig. S7c and
290 Supplementary Movie 2), therefore we propose that the hydration pocket form by T33 and a few
291 other polar residues is the entry site of the proposed Na⁺ translocation pathway. Note that we did
292 not observe a continuous hydration or Na⁺ translocation pathway to connect the periplasmic side
293 and the Na⁺ site 2, probably because this structure was in the self-inhibited plugged state and the
294 simulation time (1 μs) was also much shorter than the timescale of channel opening.

295

296 The stator unit is primed for directional rotation

297 Having analyzed the ion selectivity mechanism of the stator unit family in the context of the high-
298 resolution map of PomAB, we next sought to understand the structural basis of the rotational
299 direction of the stator unit. Cryo-ET studies in *V. alginolyticus* and *Borrelia burgdorferi* basal
300 bodies reveal that when the motor rotates in the CCW direction, its C-ring component FliG
301 interacts with the stator unit cytoplasmic domain proximal side (the side facing the motor axis);
302 while, when the motor is locked and rotates in the CW direction, FliG interacts with stator unit
303 cytoplasmic domain distal side. The motor directional switching from CCW to CW rotation
304 requires remodeling and expansion of the C-ring by changing its conformation upon receiving an
305 intracellular chemotaxis signal^{40,41}. Thus, the stator unit can drive both CW and CCW rotation of
306 the flagellar motor with a relatively fixed position by anchoring itself to the peptidoglycan layer
307 through the PGB motif.

308 Viewed from the plane of the inner membrane, we observe that the bulky hydrophobic side chain
309 of M155 from PomA chain 2 is orientated horizontally to the engaged PomB D24 (Fig. 4b),
310 revealing that M155 will sterically hinder PomA to CCW rotation around PomB at the engaged
311 D24 site (Fig. 4d). Meanwhile, M155 from PomA chain 4 elevates its side chain to stride over the
312 disengaged D24, for which the interaction with PomA is nearly absent, providing the required
313 space for D24 to gather the Na⁺ ion from the selectivity cavity (Fig. 4b, 4d). We hypothesized that
314 the bulky side chain of PomA position 155 is the stator unit directional rotation ‘reinforcement’
315 point. To test this hypothesis and verify the importance of the bulky side chain at this position, we
316 first substituted this methionine residue with alanine. The M155A mutation abolished bacterial
317 motility. In contrast, the replacement of methionine with leucine, a residue in the equivalent



318

319 **Fig. 4 VaPomAB assembly interface and its directional rotation.**

320 **a**, VaPomAB assembly interface at the periplasmic space and transmembrane domain levels, with surface colored
 321 according to hydrophobicity. For clarity, the front two chains are deleted and PomB chains are shown as ribbon. **b**,
 322 Conformational isomers of M155 near PomB engaged D24 and disengaged D24. EM densities are overlaid on the
 323 side chain of M155. **c**, Comparison of motility ability of the VaPotAB constructs and point mutants of the residue
 324 M155, and residues from PomB near M155. **d**, Conformational isomers of M155 viewed from the top of the
 membrane. The solid circle indicates the rotational direction of PomA around PomB. A potential clash that would
 occur if PomA rotated CCW around PomB is indicated with a red heptagon.

325 position often seen in H⁺-driven stator units, retained 80% motility. Increasing the size of the
 326 residues near PomA M155 from PomB (PomB F22Y and L25F) impaired motility (Fig. 4c).
 327 Therefore, our structural analysis and functional data confirm that a residue with a bulky side chain
 328 near the ion coupling site (D24 in PomB) is required to permit the correct rotation direction of the
 329 stator unit. Its conformational isomer (Extended Data Fig. S10), likely induced by the local
 330 structural rearrangement during the stator unit activation, is necessary to achieve flexibility in this
 331 region for ion transportation. This bulky hydrophobic residue is conserved not only in flagellar
 332 stator units, but also in other 5:2 rotary motors⁵², suggesting a similar directional rotation
 333 ‘reinforcement’ mechanism (Extended Data Fig. S11). The stator unit is thus a preset CW rotary
 334 motor, which is tightly blocked by the trans mode conformation of the PomB plug motif at the
 335 periplasmic level before it incorporates onto the rotor. The geometry of the stator unit will not

336 favor a model where PomA rotates CCW around PomB, when the ion motive force is reversed,
337 due to the structural clashes (Fig. 4d) and negative electrostatic potential of PomA cytoplasmic
338 inner lumen. This is consistent with early experiments showing that the stator unit is inactivated
339 when the IMF is dissipated or reversed⁵³, and that increased sodium concentration in the cytoplasm
340 inhibits the rotation of PomAB⁴⁶.

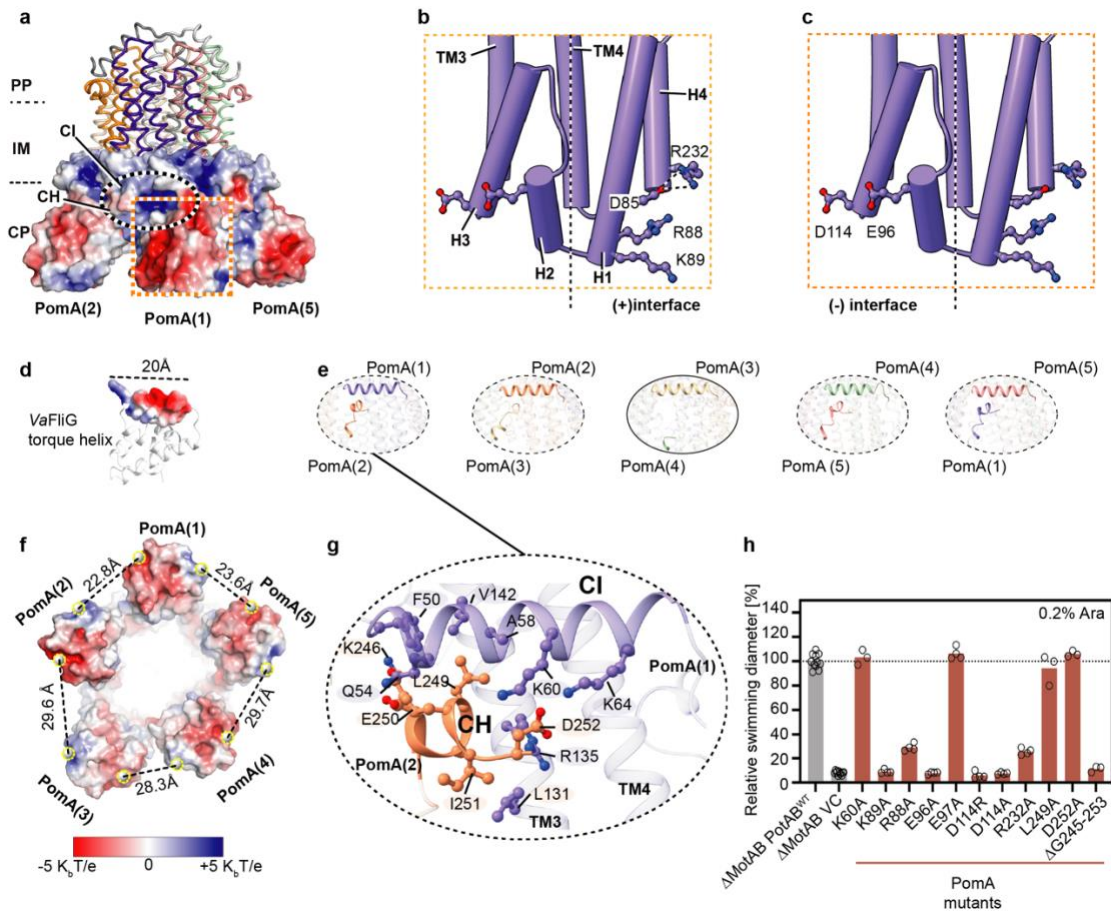
341

342 PomA cytoplasmic domain and C-terminal helical motif

343 The stator unit cytoplasmic domain plays a crucial role during rotor incorporation, torque
344 generation, and disassembly from the rotor^{1,42}. The cytoplasmic domain of each PomA subunit
345 contains four short helices that are almost vertical to the inner membrane. They peripherally
346 surround the intracellular part of the PomA TM3 and TM4 helices and together form a compact
347 helical bundle that protrudes approximately 35 Å into the cytosol (Fig. 5a-c). The cytoplasmic
348 domains from five PomA subunits diverge towards their intracellular end, with the local resolution
349 of this region decreasing considerably compared to the TMD. This is in line with the model B-
350 factor distribution, where the PomAB cytoplasmic domain has a higher B-factor value (Extended
351 Data Fig. S12), reflecting the flexibility of this region. The rotary stator unit generates torque by
352 matching the complementary charged residues with the rotor FliG torque helix. This torque-
353 generating mode is predicted to be conserved across bacterial species^{24,26,54}. We divided the FliG
354 torque helix-binding interface from the stator unit as follows: positively charged residues from one
355 PomA subunit contribute to the principal face or (+) face, and negatively charged residues from
356 the neighboring PomA subunit mainly contribute to the complementary face or (-) face (Fig. 5b-
357 c). The PomAB structure allows us to map the locations of those key residues involved in stator
358 rotor interaction. We found three positively charged residues from H1 and H4 at the (+) face, R88,
359 K89, and R232, and two negatively charged residues from H2 and H3 at the (-) face, D114 and E96,
360 that when the charge is suppressed or reversed, greatly impair motility (Fig. 5h). Importantly, the
361 charge of R88 at the (+) face and D114 and E96 at the (-) face, whose side chains project toward
362 the PomA intersubunit junction, are indispensable for motility, confirming that both (+) and (-)
363 sides of PomA are necessary and directly involved in the interactions with FliG torque helix.
364 Besides, R232 establishes an interdomain salt bridge with residue D85, and it is unlikely involved
365 in the binding with FliG torque helix, rather, stabilizing helix bundle organization (Fig. 5b).

366 Unexpectedly, we found a helical (CH) motif right after the H4 helix in the PomA C-terminal part.
367 The CH motif runs parallel to the membrane plane and attaches to the CI helix of a neighboring
368 PomA subunit. In four PomA subunits, we could trace the entire CH motifs from residue K246 to
369 its C-terminal end D253, with the contact between the CH and CI mainly mediated by electrostatic
370 and hydrophobic interactions (Fig. 5g). The remaining CH motif is disordered, without any
371 featured density observed (Fig. 5e). This disordered CH motif likely stems from the asymmetry of
372 the PomAB assembly, where there are two PomA subunits on one side of PomB plug motifs and
373 three on the other side and there is less space for this CH motif to interact with the neighboring
374 PomA CI helix. The detachment of CH from CI at one intersubunit site results in the cytoplasmic

375 domains of PomA forming an irregular pentagon, as shown by measuring distances of those charge
 376 residues responsible for FliG torque helix binding (the center of mass of K89 and R88 to the center
 377 of mass of D114 and E96) (Fig. 5f). The PomA C-terminal region is less conserved in length and
 378 sequence among stator unit subtypes (Extended Data Fig. S1b). We made a PomA C-terminal end
 379 truncation and found that PomA CH motif truncation completely abolished motility (Fig. 5h).
 380 Based on these findings and our structural analysis, we confirm that the PomA CH motif and the
 381 CH-CI interaction are critical to sustain stator unit function.



382

383 **Fig. 5 PomA cytoplasmic domain and C-terminal helical motif.**

384 **a**, PomAB cytoplasmic domain electrostatic potential. **b**, Locations of key residues responsible for FliG torque
 385 helix binding, highlighting the positively charged residues from the principal interface. **c**, Similar to **b**,
 386 but highlighting the negatively charged residues from the complementary interface. **d**, VaFliG C-terminal domain
 387 (based on homology modeling) containing the torque-generating helix is shown, and its length is indicated. **e**,
 Interactions between PomA CH helix and CI helix. One site without interaction is highlighted and circled with
 a solid line. **f**, Image from **a** viewed from the cytoplasmic domain. Distances between the center of mass of the
 residues K89, R88 and the center of mass of the residues D114, E96 from adjacent PomA subunits are given. **g**,
 Detailed interactions between CH motif and CI helix. Residues involved in interactions are shown as sticks. **h**,
 Comparison of motility ability of the VaPotAB constructs and point mutants of the residues involved in FliG
 torque helix interaction or PomA C-terminal truncation.

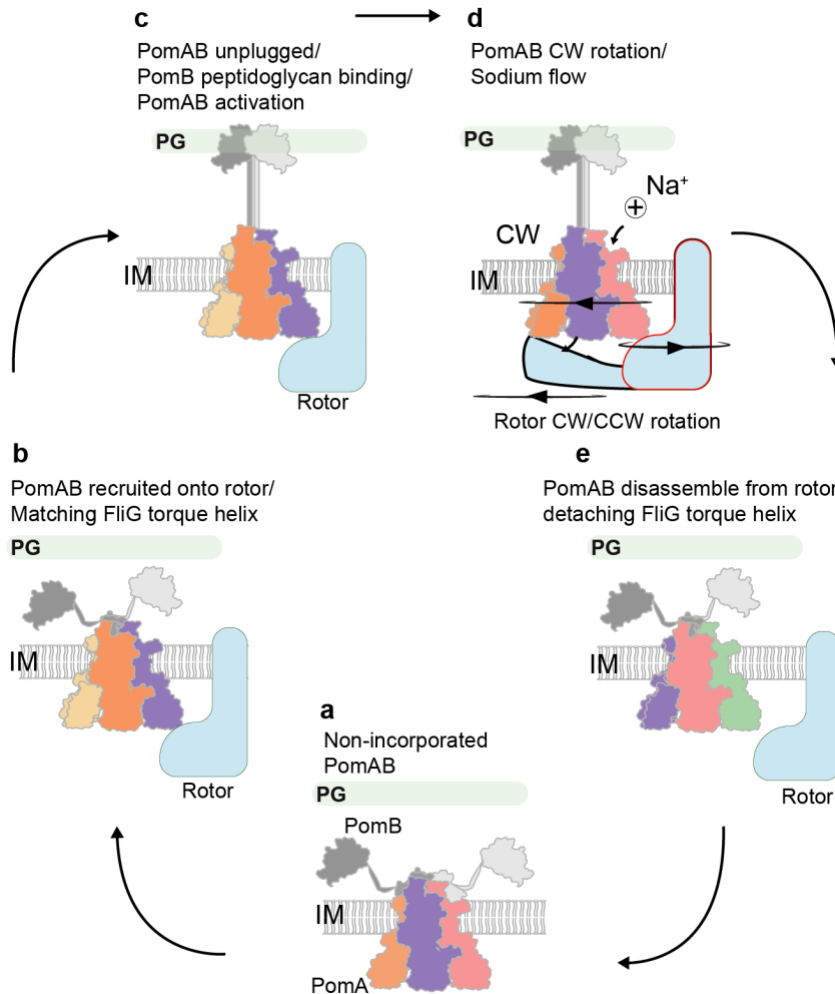
388 Discussion

389 Since it was first revealed in a marine *Vibrio* species that its flagellar motor is driven by sodium-
390 motive force^{19,55}, the Na⁺-driven stator unit has been under intense functional and structural
391 investigations for decades.

392 The trans conformation of the plug motifs seems to be a universal feature among the stator unit
393 family and their structural configuration explains how this organization tightly restrain the rotation
394 of the stator unit (Extended Data Fig. S13). The plug motifs also prevent ion influx into the
395 cytoplasmic domain before the stator unit incorporates onto the rotor. Their distinct interaction
396 environments caused by the imbalanced PomA₅:PomB₂ subunit stoichiometry also suggest their
397 asymmetric release during the stator-rotor incorporation. The signal that promotes the periplasmic
398 plug motif release is probably triggered by the cytoplasmic stator unit-rotor interaction upon the
399 incorporation of the stator units into the motor, with the signal transmission route likely being
400 through PomA transmembrane peripheral helices, particularly those two dynamic PomA TM1
401 helices. Plug motif release could then facilitate PomB PGB motifs dimerization, which can reach
402 and anchor to the cell wall through recognition of the peptidoglycan components by the dimerized
403 PGB interfacial groove, and this will produce a spatial tension preventing rebinding of the released
404 plug motif to the activated stator unit. Therefore, only the rotor-incorporated unplugged stator units
405 represent their fully activated states. Indeed, we were unable to purify the unplugged PomAB after
406 deleting the PomB plug motif. Likely, the plug deletion PomAB complex did not assemble well
407 and was toxic to the cells due to ion leakage, and the unplugged PomAB is more stable upon rotor
408 incorporation.

409 The ion permeation pathway identified in the PomAB structure provides an energy advantage by
410 shortening the sodium ion translocation path from the periplasmic side to the key ion-accepting
411 residue PomB D24. PomB S27, a polar residue right above D24, may increase solvent accessibility
412 (Fig. 3d). Additionally, the hydrophobic residues found at the periplasmic assembly interface of
413 PomA and PomB may block the ion from flowing back to the periplasmic space, and they may
414 also stabilize the stator unit by preventing it from falling apart during the stator unit's dwell on the
415 rotor (Fig. 4a). A recent study showed that when *E. coli* MotAB is replaced with an engineered
416 PomAB (PomB PGB replaced with *E. coli* MotB PGB), at a low Na⁺ environment, the engineered
417 PomAB can rapidly incorporate mutations, restoring the bacterial motility⁵⁶ and reflect the
418 adaptability of the stator unit. This is consistent with our results, where those mutations in the
419 *VaPotAB* (PomB PGB replaced with *S. enterica* MotB PGB) granted the stator unit a gain-of-
420 function phenotype in *S. enterica* (Extended Data Fig. S14a-b). Most of those mutation sites reside
421 near the ion selectivity cavity (Extended Data Fig. S14c-d), including PomB G20, L28 and PomA
422 L183, and upon mutation may modulate the ion specificity, probably enabling the stator unit to
423 use both Na⁺ and H⁺ as coupling ions. Of note, in the H⁺-driven stator unit *C. jejuni* MotAB, the
424 equivalent site of PomA L183 is phenylalanine (*CjMotA186*), whose side chain adopts two
425 conformations in the activated stator unit, affecting H⁺ translocation efficiency³⁵. We also noticed
426 that PomB L36Q has a gain-of-function phenotype. In the plugged PomAB structure, PomB chain1

427 L36 hydrophobically interacts with PomB chain 2 plug motif F47 (not PomB chain2 L36 with
 428 PomB chain 1 F47, due to asymmetric assembly) (Extended Data Fig. S8g-i). The L36Q mutation
 429 possibly decreases the plug motif binding energy and makes the stator unit more activable.
 430 Additionally, it is unlikely that PomB L36 lines the previously proposed ion translocation pathway
 431 in which it forms the dehydration gate with nearby hydrophobic residues^{57,58}, as the L36A mutant
 432 has the same motility as the wild type phenotype (Extended Data Fig. S14a).



433

434

Fig. 6 Models of PomAB activation and disassembly from rotor.

435

436

437

438

439

440

a, An inactive stator unit is plugged autoinhibited. **b**, Inactive stator unit orients its cytoplasmic domain towards the rotor to contact FliG torque helix. **c**, The signal from the interaction between stator unit and rotor is transferred to the PomAB periplasmic domain, where it promotes the plug motifs release, followed by PomB PGB motifs dimerization and binding to the peptidoglycan layer. PomAB gets activated. **d**, In the activated PomAB, a sodium ion (represented by a sphere with a + symbol) passes through the PomA selectivity bind filter, and binds to PomB Asp24, triggering CW rotation of PomA around PomB. The rotor could rotate either CW or CCW direction, depending on how it interacts with the stator unit. **e**, Stator unit disassembly from the rotor when external torque is decreased.

441 The observed CH-CI interactions and the detachment in one site as well as the irregular pentagonal
442 shape of PomA cytoplasmic domain likely contribute to the process of stator unit assembly onto
443 the rotor. We propose the following model for the dynamic stator unit binding to the rotor, in which
444 the stator unit randomly orients towards the rotor and ‘measures’ the length of the FliG torque
445 helix. Once both principal and complementary faces of the PomA cytoplasmic domain catch the
446 FliG torque helix, possibly through (one of) the two shortest sites among five, which fit the length
447 of FliG torque helix best (Fig. 5d, 5f), the stator unit is incorporated and is activated (Fig. 6a-c).
448 This process could be assisted by FliL, a membrane protein recently shown to enhance the stator-
449 rotor incorporation and stabilize the stator unit in its activated form^{59,60}. During the activation, each
450 PomA subunit near the disengaged PomB D24 supplies a Na⁺ from the ion selectivity cavity to
451 couple the disengaged D24 with a Na⁺. Meanwhile, the engaged PomB D24 releases the coupled
452 Na⁺ and together with M155 ensures CW rotation of PomA around PomB as viewed from outside
453 of the membrane. At the same time, PomA cytoplasmic domain progressively interact with the
454 FliG torque helix. The rotor will either be in CCW or CW rotation mode, depending on the
455 conformation of the C-ring (Fig. 6d).

456 Given the fact that stator units constantly assemble and disassemble around the rotor, depending
457 on the requirement of external load, the asymmetric PomA cytoplasmic domain could also be
458 advantageous for the deactivated stator unit to detach from the rotor. When the external load is
459 decreased, which likely promotes the PGB motif of the PomB to disconnect from the cell wall, the
460 plug motifs of the stator unit rebind to their inhibitory sites. This signal will transfer to the stator
461 unit cytoplasmic domain, leading to its asymmetry and weakening the interactions between the
462 stator unit and rotor, promoting the stator unit to separate from the rotor (Fig. 6e). The proposed
463 model is reminiscent of the recently proposed ‘catch-bond’ mechanism, in which the
464 interaction/bond becomes weaker under reduced force and is enhanced by rotation of the rotor^{61,62}.
465 However, the atomic structure of the whole flagellar motor with the assembled stator units is
466 needed to fully understand the stator unit rotor incorporation mechanism and whether the
467 asymmetric PomA cytoplasmic domain becomes symmetric during activation remains to be further
468 investigated (Extended Data Fig. S15a-b).

469 In summary, we present the structures of *VaPomAB* in both detergent and lipidic environments.
470 The cryo-EM maps not only provide a detailed structure assembly of the Na⁺-driven stator unit,
471 but also enable us to assign the ion binding sites, which in turn allows us to address the enigmatic
472 mechanism of stator unit ion selectivity. Our structural analysis and functional experiments support
473 that the stator unit is a CW unidirectional rotary motor and this is achieved by a hydrophobic
474 directional rotation ‘reinforcement’ point. The PomB plug motifs organization and discovery of
475 PomA C-terminal helical motif further expand our view about the stator unit activation and rotor
476 incorporation.

477 **Materials and methods**

478 ***VaPomAB* purification with LMNG detergent**

479 The DNA sequence coding for *VaPomAB* was amplified from *Vibrio alginolyticus* (ATCC 17749)
480 and subcloned into a modified pET vector containing a C-terminal twin-Strep-tag. A human
481 rhinovirus (HRV) 3C protease cleavage site (GTLEVLFGQPGGS) was inserted between the
482 PomB plug motif and the peptidoglycan binding domain (between residues Gln95 and Gln96).
483 PomAB complex was expressed in *E. coli* Overexpress™ C43(DE3) cells (LuBioScience GmbH).
484 Cells were cultured in 8 l LB medium supplemented with 50 µg/ml ampicillin at 37°C, and protein
485 expression was induced with 0.5 mM IPTG at OD₆₀₀ 0.6. Cells were incubated for another 16 hours
486 at 20°C before harvesting. The cell pellet was resuspended in buffer A (20 mM HEPES pH 7.5,
487 300 mM NaCl) with 30 µg/ml of DNase I and 50 µg/ml of lysozyme and incubated at 4°C for 30
488 min before passing it through an EmulsiFlex-C5 homogenizer at 15,000-20,000 pound-force per
489 square inch. Unbroken cells were removed by centrifugation at 8000 rpm for 15 min. Membranes
490 were then sedimented at 41,000 rpm for 1 hour and stored at -20°C after flash freezing with liquid
491 nitrogen.

492 For protein purification, membranes were solubilized in buffer A supplemented with 2% (w/v)
493 Lauryl Maltose Neopentyl Glycol (LMNG), 10% glycerol, and protease inhibitors (protease
494 inhibitor cocktail tablets, EDTA-free, Roche Diagnostics GmbH) for 2 hours at 4°C while shaking
495 on a rocking platform, and then ultracentrifuged for 30 min at 28,000 rpm. The supernatant was
496 added to a gravity flow column containing 2 ml Strep-Tactin® Superflow® resin (IBA) pre-
497 equilibrated with washing buffer (buffer A with 10% glycerol and 0.005% LMNG). Resins were
498 washed five times with 4 column volumes of washing buffer and Strep tagged protein was eluted
499 with elution buffer (Buffer A, 10% glycerol, 0.005% LMNG and 10 mM desthiobiotin). The
500 protein complex was then concentrated until reaching a volume of 0.5 ml. HRV-3C protease was
501 added to the *VaPomAB* sample, with a protein:protease ratio of 5:1 (w/w) and incubated at 4°C
502 overnight. The sample was loaded onto a Superose® 6 Increase 10/300 GL (Merck) column, pre-
503 equilibrated with buffer A with 0.002% LMNG. The peak fractions corresponding to the protein
504 complex were concentrated to about 16-20 mg/ml using a centrifugal filter with a PES membrane
505 (Sartorius) and used for preparation of cryo-EM sample grids immediately.

506 ***VaPomAB* MSP1D1 and Saposin lipid nanodisc reconstitution**

507 To reconstitute *VaPomAB* into lipid nanodiscs with MSP1D1, 500 µl of 2 mg/ml purified
508 *VaPomAB* without PomB PGB was mixed with *E. coli* polar lipids and MSP1D1 in a molar ratio
509 of 1:156:6.25 (*VaPomAB*:lipids:MSP1D1). The reaction was incubated at 4°C with mild agitation
510 for 5 min. Bio-beads (300 mg per ml reaction) were added and incubated overnight to remove the
511 detergent. Bio-beads were filtered out the next day using a PVDF 0.22 µm Centrifugal Filter
512 (Durapore) tube. The sample was then injected into a Superose® 6 Increase 10/300 GL (Merck)
513 column, which was pre-equilibrated with buffer A. The peak fractions corresponding to the protein

514 complex in lipid nanodiscs of MSP1D1 were pooled, concentrated and used for cryo-EM grids
515 preparation.

516 To reconstitute *VaPomAB* into lipid nanodiscs with saposin, 300 μ l of 6 mg/ml full length purified
517 *VaPomAB* (without protease insertion) was mixed with *E. coli* polar lipids (10 mM; 200 μ l) and
518 incubated at room temperature for 10 min. Saposin (6.7 mg/ml; 350 μ l) was added into the reaction
519 and incubated for 2 min. The molar ratio of *PomAB*, lipids and saposin was 1:300:35, respectively.
520 The reaction was diluted with 2 ml buffer A to initiate the reconstitution and incubated on ice for
521 an additional 30 min. 700 mg of bio-beads were added and incubated overnight to remove the
522 detergent. The rest of the steps were the same as when *VaPomAB* was reconstituted into MSP1D1
523 nanodiscs.

524 Cryo-EM grids preparation and cryo-EM data collection

525 To break the preferential particle orientation, 0.0125% CHAPSO (final concentration) was added
526 into the sample before grid preparation. 2.7 μ l of freshly purified sample was applied onto glow-
527 discharged (30 s, 5 mA) grids (Quantifoil R 0.6/1 300 mesh Cu or Ultrafoil 0.6/1 300 mesh Au)
528 and plunge-frozen into liquid ethane using a Vitrobot Mark IV (FEI, Thermo Fisher Scientific)
529 with the following parameters: 4°C, 100% humidity, 7 s wait time, 4-4.5 s blot time, and a blot
530 force of 25. Movies were collected using the semi-automated acquisition program EPU (FEI,
531 Thermo Fisher Scientific) on a Titan Krios G2 microscope operated at 300 keV paired with a
532 Falcon 3EC direct electron detector (FEI, Thermo Fisher Scientific). Images were recorded in an
533 electron counting mode, at 96,000x magnification with a calibrated pixel size of 0.832 Å and
534 defocus range of 0.8 to 3 μ M. For the *VaPomAB* sample purified in LMNG, 6,467 micrographs
535 were collected, with each micrograph containing 40 frames and a total exposure dose of 37.98
536 ($e/\text{Å}^2$). For the *VaPomAB* sample reconstituted into saposin nanodiscs, 3,927 micrographs were
537 collected, with each micrograph containing 40 frames and a total exposure dose of 37 ($e/\text{Å}^2$). For
538 the *VaPomAB* MSP1D1 sample, 5,450 micrographs were collected, with each micrograph
539 containing 40 frames and a total exposure dose of 40 ($e/\text{Å}^2$).

540 Image processing

541 To keep the image data processing consistent, all the datasets were processed using cryoSPARC
542 version 3.3.2, unless otherwise stated. Patch motion correction was used to estimate and correct
543 frame motion and sample deformation (local motion). Patch Contrast function (CTF) estimation
544 was used to fit local CTF to micrographs. Micrographs were manually curated to remove the bad
545 ones (relatively ice thickness thicker than 1.05 and CTF value worse than 3.2 Å for LMNG dataset;
546 relatively ice thickness thicker than 1.1 and CTF value worse than 5 Å for MSP1D1 nanodisc
547 dataset; relatively ice thickness thicker than 1.2 and CTF value worse than 5 Å for Saposin
548 nanodisc dataset). Particles were picked using the Topaz software implemented in cryoSPARC⁶³.
549 Basically, Topaz extract was used with a pre-trained model with a pre-tested particle threshold
550 value. Particles were extracted with a box size of 400 pixels and Fourier crop to box size of 100
551 pixels. Duplicated particles were removed using a minimum separation distance criteria of 60 Å,

552 which means that the distance between the centers of two neighboring particles should be larger
553 than 60 Å. One round of 2D classification was then performed, followed by ab-initio
554 reconstruction. Heterogeneous refinement was used to get rid of the junk particles. Particles were
555 re-extracted with full box size (400 pixels). Non-uniform refinement was applied with a dynamic
556 mask to obtain a high-resolution map. Local refinement was additionally performed with a soft
557 mask surrounding VaPomAB complex in order to achieve a higher resolution map. The number of
558 micrographs, total exposure values, number of particles used for final refinement, and map
559 resolution values for all datasets are summarized in Table S1.

560 Atomic model building, refinement, and validation

561 ColabFold⁶⁴ was used to predict the structure of PomA pentamer⁶⁵ and manually fit the model
562 into the density by using UCSF ChimeraX⁶⁶. The model was refined in Coot⁶⁷, and PomB TM
563 and plug motif was manually modelled. The model was then refined against the map using
564 PHENIX real space refinement⁶⁸.

565 Molecular dynamics simulation of PomAB

566 The system was constructed by embedding the cryo-EM structure of PomAB into a flat, mixed
567 lipid bilayer consisting of 16:0-18:1 phosphatidylethanolamine (POPE) and 1-palmitoyl-2-oleoyl
568 phosphatidylglycerol (POPG) at a 4:1 ratio using the Membrane Builder tool of CHARMM-GUI
569 webserver⁶⁹. Explicit water was added using the TIP3P water model, and the system charge was
570 neutralized with sodium ions and solvated in a cubic water box containing 0.15 M NaCl. The size
571 of the box was 11.0 nm, 11.0 nm, and 11.5 nm in the x, y and z dimension, respectively, resulting
572 in ~144,000 atoms in total. The CHARMM36m force field⁷⁰ was used for the protein, and the
573 CHARMM36 lipid force field⁷¹ was used for all lipid molecules. Note that the WYF correction
574 was included in the force field to improve the description of the cation- π interactions⁷². The
575 temperature was kept constant at 310 K using the V-rescale algorithm with a 2 ps coupling constant,
576 and the pressure at 1.0 bar using the Parrinello-Rahman barostat⁷³ with a 5 ps time coupling
577 constant. A cutoff of 1.2 nm was applied for the van der Waals interactions using a switch function
578 starting at 1.0 nm. The cutoff for the short-range electrostatic interactions was also at 1.2 nm and
579 the long-range electrostatic interactions were calculated by means of the particle mesh Ewald
580 decomposition algorithm with a 0.12 nm mesh spacing. A reciprocal grid of 96 x 96 x 96 cells was
581 used with 4th order B-spline interpolation. MD simulations were performed using Gromacs2021.5
582⁷⁴. Two independent simulations were performed, each for one μ s. Analysis of the MD trajectories
583 was performed using the Gromacs gmx and GROmaps tools⁷⁵.

584 Bacterial strains and growth

585 *Escherichia coli* and *Salmonella enterica* serovar *Typhimurium* LT2 (J. Roth) (ATCC 700720)
586 were grown at 37°C with aeration at 180 rpm in lysogeny broth (LB medium) [10 g/l tryptone, 5
587 g/l yeast extract and 5 g/l NaCl]. For solid agar plates, 1.5% (w/v) of agar-agar was added,
588 alternatively to test swimming motility 0.3% (w/v) of agar-agar was supplemented. All strains
589 used in this study are listed in the supplement information Table S2. For strains harboring a

590 plasmid carrying a resistance marker selected media were supplemented with chloramphenicol
591 (12.5 µg/ml). Induction experiments were performed in the presence of arabinose (0.2%).

592 DNA manipulation

593 Plasmids were constructed according to standard cloning techniques as described elsewhere (ISBN
594 0879695773). In brief, rolling circle, around the horn PCR and overlap PCR were applied to
595 generate point mutations in *pomA* or *pomB*, respectively. The primers used in this study are listed
596 in the supplement information Table S3. For DNA amplification Q5 polymerase was used and for
597 verification OneTaq polymerase (both purchased from NEB, Ipswich, MA, USA). All plasmids
598 were verified by sequencing.

599 Motility assay

600 To assess the swimming motility of *VaPotAB* mutants respective strains were inoculated in LB
601 medium supplemented with chloramphenicol. From overnight cultures, soft agar plates containing
602 the selective marker and supplemented with or without arabinose were inoculated with 2 µl and
603 incubated at 37°C. Once a decent halo was visible, plates were scanned. From these pictures
604 swimming diameters were evaluated using Fiji (10.1038/nmeth.2019).

605 Figure preparation

606 Figures were prepared using ChimeraX ⁶⁶, PyMOL, GraphPad Prism 9 and Adobe Illustrator.
607 Surface buried area and solvation free energy was calculated using the online webserver
608 PDBePISA ⁷⁶.

609

610 Data and Code Availability

611 Atomic coordinates for *VaPomAB* in LMNG detergent and *VaPomAB* in MSP1D1 nanodisc were
612 deposited in the Protein Data Bank under accession codes PDB: 8BRD and 8BRI, respectively.
613 The corresponding electrostatic potential maps were deposited in the Electron Microscopy Data
614 Bank (EMDB) under accession codes EMDB: EMD-16212 and EMD-16215, respectively. The
615 electrostatic potential map for full length *VaPomAB* in Saposin nanodisc was deposited in the
616 EMDB under accession code EMDB: EMD-16214.

617 Author contribution

618 N.M.I.T. supervised the project and acquired funding. H.H. expressed, purified, optimized,
619 prepared cryo-EM grids, collected cryo-EM data, and determined the structure of *VaPomAB* and
620 the structures of *VaPomAB* in nanodiscs. M.S. helped with protein expression, purification, and
621 cryo-EM grid preparation at the beginning of this project. P.F.P. did the motility assay and
622 interpreted data together with M.E.. W.Y. and Z.L. performed the molecular dynamics simulations.
623 M.S., A.R.-E., and Y.M.Y. helped with data analysis and figure preparation. N.W helped with data
624 interpretation. H.H. built and refined the structure models, prepared figures and wrote the first

625 draft of the manuscript with input from all the authors, which was then edited by N.M.I.T. and
626 M.E.. All authors contributed to the revision of the manuscript.

627

628 Acknowledgements

629 The Novo Nordisk Foundation Center for Protein Research is supported financially by the Novo
630 Nordisk Foundation (NNF14CC0001). N.M.I.T. acknowledges support from DFF grant (8123-
631 00002B) and NNF Hallas-Møller Emerging Investigator grant (NNF17OC0031006). M.E.
632 acknowledges support by the European Research Council (ERC) under the European Union's
633 Horizon 2020 research and innovation program (agreement no. 864971). Y.W. acknowledges the
634 financial support from National Key Research and Development Program of China (No.
635 2021YFF1200404) and the Fundamental Research Funds for the Central Universities of China (No.
636 K20220228), as well as the access to computational resources from the Information Technology
637 Center and State Key Lab of CAD&CG, ZheJiang University. H.H. acknowledges support from
638 Lundbeck Foundation postdoc R347-2020-2429. We thank the Danish Cryo-EM Facility at the
639 Core Facility for Integrated Microscopy (CFIM) at the University of Copenhagen and Tillmann
640 Pape and Nicholas Heelund Sofos for support during data collection.

641 References:

- 642 1. Hu, H. *et al.* Structural basis of torque generation in the bi-directional bacterial flagellar motor.
643 *Trends Biochem. Sci.* **0**, (2021).
- 644 2. Macnab, R. M. How bacteria assemble flagella. *Annu. Rev. Microbiol.* **57**, 77–100 (2003).
- 645 3. Minamino, T., Imada, K. & Namba, K. Molecular motors of the bacterial flagella. *Curr. Opin.*
646 *Struct. Biol.* **18**, 693–701 (2008).
- 647 4. Wadhwa, N. & Berg, H. C. Bacterial motility: machinery and mechanisms. *Nat. Rev.*
648 *Microbiol.* **20**, 161–173 (2022).
- 649 5. Berg, H. C. The Rotary Motor of Bacterial Flagella. *Annu. Rev. Biochem.* **72**, 19–54 (2003).
- 650 6. Berg, H. C. & Anderson, R. A. Bacteria Swim by Rotating their Flagellar Filaments. *Nature*
651 **245**, 380–382 (1973).
- 652 7. Minamino, T., Kinoshita, M. & Namba, K. Directional Switching Mechanism of the Bacterial
653 Flagellar Motor. *Comput. Struct. Biotechnol. J.* **17**, 1075–1081 (2019).
- 654 8. Webre, D. J., Wolanin, P. M. & Stock, J. B. Bacterial chemotaxis. *Curr. Biol.* **13**, R47–R49
655 (2003).
- 656 9. Blair, D. F. & Berg, H. C. Restoration of Torque in Defective Flagellar Motors. *Science* **242**,
657 1678–1681 (1988).
- 658 10. Khan, S., Dapice, M. & Reese, T. S. Effects of *mot* gene expression on the structure of the
659 flagellar motor. *J. Mol. Biol.* **202**, 575–584 (1988).
- 660 11. Block, S. M. & Berg, H. C. Successive incorporation of force-generating units in the bacterial
661 rotary motor. *Nature* **309**, 470–472 (1984).
- 662 12. Leake, M. C. *et al.* Stoichiometry and turnover in single, functioning membrane protein
663 complexes. *Nature* **443**, 355–358 (2006).
- 664 13. Reid, S. W. *et al.* The maximum number of torque-generating units in the flagellar motor of
665 *Escherichia coli* is at least 11. *Proc. Natl. Acad. Sci. U. S. A.* **103**, 8066–8071 (2006).
- 666 14. Antani, J. D. *et al.* Mechanosensitive recruitment of stator units promotes binding of the
667 response regulator CheY-P to the flagellar motor. *Nat. Commun.* **12**, 5442 (2021).
- 668 15. Minamino, T., Terahara, N., Kojima, S. & Namba, K. Autonomous control mechanism of
669 stator assembly in the bacterial flagellar motor in response to changes in the environment. *Mol.*
670 *Microbiol.* **109**, 723–734 (2018).
- 671 16. Wadhwa, N., Phillips, R. & Berg, H. C. Torque-dependent remodeling of the bacterial flagellar
672 motor. *Proc. Natl. Acad. Sci.* **116**, 11764–11769 (2019).
- 673 17. Wadhwa, N., Tu, Y. & Berg, H. C. Mechanosensitive remodeling of the bacterial flagellar
674 motor is independent of direction of rotation. *Proc. Natl. Acad. Sci.* **118**, e2024608118 (2021).

- 675 18. Nord, A. L. *et al.* Catch bond drives stator mechanosensitivity in the bacterial flagellar motor.
676 *Proc. Natl. Acad. Sci.* **114**, 12952–12957 (2017).
- 677 19. Asai, Y. *et al.* Putative channel components for the fast-rotating sodium-driven flagellar motor
678 of a marine bacterium. *J. Bacteriol.* **179**, 5104–5110 (1997).
- 679 20. Blair, D. F. & Berg, H. C. The MotA protein of *E. coli* is a proton-conducting component of
680 the flagellar motor. *Cell* **60**, 439–449 (1990).
- 681 21. Chang, Y., Carroll, B. L. & Liu, J. Structural basis of bacterial flagellar motor rotation and
682 switching. *Trends Microbiol.* (2021) doi:10.1016/j.tim.2021.03.009.
- 683 22. Hosking, E. R., Vogt, C., Bakker, E. P. & Manson, M. D. The *Escherichia coli* MotAB Proton
684 Channel Unplugged. *J. Mol. Biol.* **364**, 921–937 (2006).
- 685 23. Li, N., Kojima, S. & Homma, M. Characterization of the Periplasmic Region of PomB, a Na⁺-
686 Driven Flagellar Stator Protein in *Vibrio alginolyticus*. *J. Bacteriol.* **193**, 3773–3784 (2011).
- 687 24. Lloyd, S. A. & Blair, D. F. Charged residues of the rotor protein FliG essential for torque
688 generation in the flagellar motor of *Escherichia coli*. *J. Mol. Biol.* **266**, 733–744 (1997).
- 689 25. Morimoto, Y. V., Nakamura, S., Kami-ike, N., Namba, K. & Minamino, T. Charged residues
690 in the cytoplasmic loop of MotA are required for stator assembly into the bacterial flagellar
691 motor. *Mol. Microbiol.* **78**, 1117–1129 (2010).
- 692 26. Zhou, J. & Blair, D. F. Residues of the cytoplasmic domain of MotA essential for torque
693 generation in the bacterial flagellar motor. *J. Mol. Biol.* **273**, 428–439 (1997).
- 694 27. Zhou, J., Lloyd, S. A. & Blair, D. F. Electrostatic interactions between rotor and stator in the
695 bacterial flagellar motor. *Proc. Natl. Acad. Sci.* **95**, 6436–6441 (1998).
- 696 28. Imae, Y. & Atsumi, T. Na⁺-driven bacterial flagellar motors. *J. Bioenerg. Biomembr.* **21**, 705–
697 716 (1989).
- 698 29. Ito, M. *et al.* MotPS is the stator-force generator for motility of alkaliphilic *Bacillus*, and its
699 homologue is a second functional Mot in *Bacillus subtilis*. *Mol. Microbiol.* **53**, 1035–1049
700 (2004).
- 701 30. Islam, M. I., Lin, A., Lai, Y.-W., Matzke, N. J. & Baker, M. A. B. Ancestral Sequence
702 Reconstructions of MotB Are Proton-Motile and Require MotA for Motility. *Front. Microbiol.*
703 **11**, (2020).
- 704 31. Li, N., Kojima, S. & Homma, M. Sodium-driven motor of the polar flagellum in marine
705 bacteria *Vibrio*. *Genes Cells* **16**, 985–999 (2011).
- 706 32. Minamino, T. & Imada, K. The bacterial flagellar motor and its structural diversity. *Trends*
707 *Microbiol.* **23**, 267–274 (2015).

- 708 33. Terahara, N., Sano, M. & Ito, M. A Bacillus Flagellar Motor That Can Use Both Na⁺ and K⁺
709 as a Coupling Ion Is Converted by a Single Mutation to Use Only Na⁺. *PLOS ONE* **7**, e46248
710 (2012).
- 711 34. Deme, J. C. *et al.* Structures of the stator complex that drives rotation of the bacterial flagellum.
712 *Nat. Microbiol.* **5**, 1553–1564 (2020).
- 713 35. Santiveri, M. *et al.* Structure and Function of Stator Units of the Bacterial Flagellar Motor.
714 *Cell* (2020) doi:10.1016/j.cell.2020.08.016.
- 715 36. Johnson, S. *et al.* Molecular structure of the intact bacterial flagellar basal body. *Nat. Microbiol.*
716 **6**, 712–721 (2021).
- 717 37. Tan, J. *et al.* Structural basis of assembly and torque transmission of the bacterial flagellar
718 motor. *Cell* **0**, (2021).
- 719 38. Yamaguchi, T. *et al.* Structure of the molecular bushing of the bacterial flagellar motor. *Nat.*
720 *Commun.* **12**, 4469 (2021).
- 721 39. Carroll, B. L. & Liu, J. Structural Conservation and Adaptation of the Bacterial Flagella Motor.
722 *Biomolecules* **10**, 1492 (2020).
- 723 40. Chang, Y. *et al.* Structural insights into flagellar stator–rotor interactions. *eLife* **8**, e48979
724 (2019).
- 725 41. Chang, Y. *et al.* Molecular mechanism for rotational switching of the bacterial flagellar motor.
726 *Nat. Struct. Mol. Biol.* **27**, 1041–1047 (2020).
- 727 42. Takekawa, N., Imada, K. & Homma, M. Structure and Energy-Conversion Mechanism of the
728 Bacterial Na⁺-Driven Flagellar Motor. *Trends Microbiol.* **28**, 719–731 (2020).
- 729 43. Chen, J., Noble, A. J., Kang, J. Y. & Darst, S. A. Eliminating effects of particle adsorption to
730 the air/water interface in single-particle cryo-electron microscopy: Bacterial RNA polymerase
731 and CHAPSO. *J. Struct. Biol. X* **1**, 100005 (2019).
- 732 44. Kampjut, D., Steiner, J. & Sazanov, L. A. Cryo-EM grid optimization for membrane proteins.
733 *iScience* **24**, 102139 (2021).
- 734 45. Terashima, H., Kojima, S. & Homma, M. Site-Directed Cross-Linking Identifies the Stator-
735 Rotor Interaction Surfaces in a Hybrid Bacterial Flagellar Motor. *J. Bacteriol.* **203**, (2021).
- 736 46. Takekawa, N. *et al.* Na⁺ conductivity of the Na⁺-driven flagellar motor complex composed of
737 unplugged wild-type or mutant PomB with PomA. *J. Biochem. (Tokyo)* **153**, 441–451 (2013).
- 738 47. Homma, M., Terashima, H., Koiwa, H. & Kojima, S. Putative Spanner Function of the Vibrio
739 PomB Plug Region in the Stator Rotation Model for Flagellar Motor. *J. Bacteriol.* **203**,
740 e00159-21 (2021).
- 741 48. Zheng, H. *et al.* CheckMyMetal: a macromolecular metal-binding validation tool. *Acta*
742 *Crystallogr. Sect. Struct. Biol.* **73**, 223–233 (2017).

- 743 49. Nishino, Y., Onoue, Y., Kojima, S. & Homma, M. Functional chimeras of flagellar stator
744 proteins between *E. coli* MotB and *Vibrio* PomB at the periplasmic region in *Vibrio* or *E. coli*.
745 *MicrobiologyOpen* **4**, 323–331 (2015).
- 746 50. Asai, Y., Yakushi, T., Kawagishi, I. & Homma, M. Ion-coupling Determinants of Na⁺-driven
747 and H⁺-driven Flagellar Motors. *J. Mol. Biol.* **327**, 453–463 (2003).
- 748 51. Kim, S. *et al.* Transmembrane glycine zippers: Physiological and pathological roles in
749 membrane proteins. *Proc. Natl. Acad. Sci.* **102**, 14278–14283 (2005).
- 750 52. Rieu, M., Krutyholowa, R., Taylor, N. M. I. & Berry, R. M. A new class of biological ion-
751 driven rotary molecular motors with 5:2 symmetry. *Front. Microbiol.* **13**, (2022).
- 752 53. Fung, D. C. & Berg, H. C. Powering the flagellar motor of *Escherichia coli* with an external
753 voltage source. *Nature* **375**, 809–812 (1995).
- 754 54. Lee, L. K., Ginsburg, M. A., Crovace, C., Donohoe, M. & Stock, D. Structure of the torque
755 ring of the flagellar motor and the molecular basis for rotational switching. *Nature* **466**, 996–
756 1000 (2010).
- 757 55. Chernyak, B. v., Dibrov, P. a., Glagolev, A. n., Sherman, M. Yu. & Skulachev, V. p. A novel
758 type of energetics in a marine alkali-tolerant bacterium. *FEBS Lett.* **164**, 38–42 (1983).
- 759 56. Ridone, P. *et al.* The rapid evolution of flagellar ion-selectivity in experimental populations of
760 *E. coli*. 2021.01.26.427765 Preprint at <https://doi.org/10.1101/2021.01.26.427765> (2022).
- 761 57. Sudo, Y., Terashima, H., Abe-Yoshizumi, R., Kojima, S. & Homma, M. Comparative study
762 of the ion flux pathway in stator units of proton- and sodium-driven flagellar motors.
763 *BIOPHYSICS* **5**, 45–52 (2009).
- 764 58. Onoue, Y. *et al.* Essential ion binding residues for Na⁺ flow in stator complex of the *Vibrio*
765 flagellar motor. *Sci. Rep.* **9**, 11216 (2019).
- 766 59. Guo, S., Xu, H., Chang, Y., Motaleb, M. A. & Liu, J. FliL ring enhances the function of
767 periplasmic flagella. *Proc. Natl. Acad. Sci. U. S. A.* **119**, e2117245119 (2022).
- 768 60. Tachiyama, S. *et al.* The flagellar motor protein FliL forms a scaffold of circumferentially
769 positioned rings required for stator activation. *Proc. Natl. Acad. Sci.* **119**, (2022).
- 770 61. Wadhwa, N., Sassi, A., Berg, H. C. & Tu, Y. A multi-state dynamic process confers mechano-
771 adaptation to a biological nanomachine. *Nat. Commun.* **13**, 5327 (2022).
- 772 62. Ito, K. I., Nakamura, S. & Toyabe, S. Cooperative stator assembly of bacterial flagellar motor
773 mediated by rotation. *Nat. Commun.* **12**, 3218 (2021).
- 774 63. Bepler, T. *et al.* Positive-unlabeled convolutional neural networks for particle picking in cryo-
775 electron micrographs. *Nat. Methods* **16**, 1153–1160 (2019).
- 776 64. Mirdita, M. *et al.* ColabFold: making protein folding accessible to all. *Nat. Methods* **19**, 679–
777 682 (2022).

- 778 65. Jumper, J. *et al.* Highly accurate protein structure prediction with AlphaFold. *Nature* **596**, 583–
779 589 (2021).
- 780 66. Pettersen, E. F. *et al.* UCSF ChimeraX: Structure visualization for researchers, educators, and
781 developers. *Protein Sci. Publ. Protein Soc.* **30**, 70–82 (2021).
- 782 67. Emsley, P. & Cowtan, K. Coot: model-building tools for molecular graphics. *Acta Crystallogr.*
783 *D Biol. Crystallogr.* **60**, 2126–2132 (2004).
- 784 68. Liebschner, D. *et al.* Macromolecular structure determination using X-rays, neutrons and
785 electrons: recent developments in Phenix. *Acta Crystallogr. Sect. Struct. Biol.* **75**, 861–877
786 (2019).
- 787 69. Jo, S., Kim, T., Iyer, V. G. & Im, W. CHARMM-GUI: a web-based graphical user interface
788 for CHARMM. *J. Comput. Chem.* **29**, 1859–1865 (2008).
- 789 70. Huang, J. *et al.* CHARMM36m: An Improved Force Field for Folded and Intrinsically
790 Disordered Proteins. *Nat. Methods* **14**, 71–73 (2017).
- 791 71. Klauda, J. B. *et al.* Update of the CHARMM All-Atom Additive Force Field for Lipids:
792 Validation on Six Lipid Types. *J. Phys. Chem. B* **114**, 7830–7843 (2010).
- 793 72. Khan, H. M., MacKerell, A. D. Jr. & Reuter, N. Cation- π Interactions between Methylated
794 Ammonium Groups and Tryptophan in the CHARMM36 Additive Force Field. *J. Chem.*
795 *Theory Comput.* **15**, 7–12 (2019).
- 796 73. Parrinello, M. & Rahman, A. Polymorphic transitions in single crystals: A new molecular
797 dynamics method. *J. Appl. Phys.* **52**, 7182–7190 (1981).
- 798 74. Abraham, M. J. *et al.* GROMACS: High performance molecular simulations through multi-
799 level parallelism from laptops to supercomputers. *SoftwareX* **1–2**, 19–25 (2015).
- 800 75. Briones, R., Blau, C., Kutzner, C., de Groot, B. L. & Aponte-Santamaría, C. GROmaps: A
801 GROMACS-Based Toolset to Analyze Density Maps Derived from Molecular Dynamics
802 Simulations. *Biophys. J.* **116**, 4–11 (2019).
- 803 76. Krissinel, E. & Henrick, K. Inference of macromolecular assemblies from crystalline state. *J.*
804 *Mol. Biol.* **372**, 774–797 (2007).
- 805

806 **Figure legends:**

807 **Fig. 1 Cryo-EM map and overall architecture of the Na⁺-driven stator unit *VaPomAB*.**

808 **a**, Cryo-EM map of *VaPomAB*. PomA subunits (purple, orange, yellow, green and red) surround
809 PomB subunits (black and white) viewed from the plane of the membrane. Dashed lines represent
810 approximate inner membrane boundaries. **b**, Cryo-EM map of *VaPomAB* viewed from the
811 periplasmic side. **c**, Ribbon model representation of *VaPomAB*. Subunits are colored as in **a**. **d**,
812 *VaPomAB* model viewed from the periplasmic side. **e**, Local resolution map of *VaPomAB* viewed
813 from a cross section as indicated in **a**. **f**, Topology diagram and secondary structural elements of
814 *VaPomA* (purple) and *VaPomB* (black) subunits. The gray ellipse indicates the PomB
815 peptidoglycan-binding domain (PGB). Abbreviations: PP, periplasm; IM, inner membrane; CP,
816 cytoplasm; PG, peptidoglycan; TM, transmembrane; H, helix.

817

818 **Fig. 2 PomB plug motif and auto-inhibition mechanism.**

819 **a**, *VaPomAB* in its auto-inhibited state, viewed from the plane of the membrane, with PomB shown
820 as ribbons (black and white) and PomA shown as a semitransparent surface representation. The
821 aspartate residues D24 from both PomB TM are indicated and shown as sticks. **b**, Top view of
822 *VaPomAB* with PomB shown as ribbons and PomA shown as a surface representation colored
823 according to its hydrophobicity. **c**, Top view of *VaPomAB*. PomA subunits are shown as a surface
824 representation and PomB subunits are displayed as ribbons, colored as in Fig. 1**a**. **d**, Close-up view
825 from the periplasmic side of the interactions of the linkers (Phe39-Asp43) that connect PomB plug
826 motifs and TMs (it corresponds to the yellow box in **c**). Hydrogen bonds are represented as dashed
827 lines. **e**, Plug motif from PomB(2) binding environment (black box in **c**). **f**, Plug motif from
828 PomB(1) binding environment (red box in **c**). **g-h**, Calculated interface buried area and free energy
829 of PomB plug motifs.

830

831 **Fig. 3 Ion binding sites, selectivity, and translocation pathway.**

832 **a**, Cross section view (corresponding to the view in left panel and rotated 90°) of Na⁺ ion binding
833 sites (cyan spheres) in the vicinities of the two Asp24 from PomB. **b**, Details of the Na⁺ ion binding
834 site near PomB(1) engaged Asp24. For clarity, corresponding EM densities are only overlapped in
835 the region of PomB(1) Gly20-Asp24, Na⁺ ion, and water molecule. Hydrogen bonds are indicated
836 as dashed lines with distances in angstroms. **c**, Details of the Na⁺ ion binding site near disengaged
837 PomB(2) Asp24. EM density is overlaid on the Na⁺ ion. **d**, Na⁺ ion translocation pathway (dashed
838 line with arrow). Periplasmic and cytoplasmic channels are indicated, with surface colored by
839 electrostatic potential (positively charged, blue; negatively charged, red). C α atoms of the residues
840 forming the putative hydrophobic gate, of the glycines forming the glycine zipper motif, and of
841 the PomB (2) S27 and D24 C α are indicated and shown as spheres **e**, Top view of the Na⁺ ion
842 translocation pathway. **f**, *VaPomAB* sodium ion binding environment near the engaged site. The

843 surface of PomA is colored by hydrophobicity. **g**, Similar view as in **f**, but in the proton-driven
844 stator unit *CjMotAB*. **h**, Similar view as in **f**, but in the proton-driven stator unit *BsMotAB*. **i**,
845 Comparison of motility ability of the *VaPotAB* constructs and point mutants of the residues near
846 the Na⁺ ion binding site or residues along Na⁺ translocation pathway.

847

848 **Fig. 4 *VaPomAB* assembly interface and its directional rotation.**

849 **a**, *VaPomAB* assembly interface at the periplasmic space and transmembrane domain levels, with
850 surface colored according to hydrophobicity. For clarity, the front two chains are deleted and
851 PomB chains are shown as ribbon. **b**, Conformational isomers of M155 near PomB engaged D24
852 and disengaged D24. EM densities are overlaid on the side chain of M155. **c**, Comparison of
853 motility ability of the *VaPotAB* constructs and point mutants of the residue M155, and residues
854 from PomB near M155. **d**, Conformational isomers of M155 viewed from the top of the membrane.
855 The solid circle indicates the rotational direction of PomA around PomB. A potential clash that
856 would occur if PomA rotated CCW around PomB is indicated with a red heptagon.

857

858 **Fig. 5 PomA cytoplasmic domain and C-terminal helical motif.**

859 **a**, PomAB cytoplasmic domain electrostatic potential. **b**, Locations of key residues responsible for
860 FliG torque helix binding, highlighting the positively charged residues from the principal interface.
861 **c**, Similar to **b**, but highlighting the negatively charged residues from the complementary interface.
862 **d**, *VaFliG* C-terminal domain (based on homology modeling) containing the torque-generating
863 helix is shown, and its length is indicated. **e**, Interactions between PomA CH helix and CI helix.
864 One site without interaction is highlighted and circled with a solid line. **f**, Image from **a** viewed
865 from the cytoplasmic domain. Distances between the center of mass of the residues K89, R88 and
866 the center of mass of the residues D114, E96 from adjacent PomA subunits are given. **g**, Detailed
867 interactions between CH motif and CI helix. Residues involved in interactions are shown as sticks.
868 **h**, Comparison of motility ability of the *VaPotAB* constructs and point mutants of the residues
869 involved in FliG torque helix interaction or PomA C-terminal truncation.

870

871 **Fig. 6 Models of PomAB activation and disassembly from rotor.**

872 **a**, An inactive stator unit is plugged autoinhibited. **b**, Inactive stator unit orients its cytoplasmic
873 domain towards the rotor to contact FliG torque helix. **c**, The signal from the interaction between
874 stator unit and rotor is transferred to the PomAB periplasmic domain, where it promotes the plug
875 motifs release, followed by PomB PGB motifs dimerization and binding to the peptidoglycan layer.
876 PomAB gets activated. **d**, In the activated PomAB, a sodium ion (represented by a sphere with a
877 + symbol) passes through the PomA selectivity bind filter, and binds to PomB Asp24, triggering
878 CW rotation of PomA around PomB. The rotor could rotate either CW or CCW direction,

879 depending on how it interacts with the stator unit. **e**, Stator unit disassembly from the rotor when
880 external torque is decreased.

881

882 **Fig. S1 Protein sequence alignment of *VaPomA* and *VaPomB* homologs from different**
883 **bacterial species.**

884 **a-b**, Multiple-sequence alignment of PomA (**a**) and PomB (**b**). The proteins are grouped into two
885 families: sodium- and proton- driven stator units. In the case of *CsMotAB*, whose cryo-EM
886 structure is available, the ion type is ambiguous, and therefore it is labeled with a question mark.
887 *VaPomAB* residue numbers (in red) are given above the sequences. Helices are indicated by solid
888 boxes. Residues that are identical or partially conserved are highlighted in red and orange,
889 respectively. Residues that are critical for sodium ion selectivity in PomAB (T158, T185 and T186)
890 are marked with a star. Dashed line above the PomB sequence indicates that the structure was not
891 resolved in the PomAB complex cryo-EM map. PomB PGB domain is also indicated above the
892 sequence alignment. PomA C-terminal helical motif is highlighted by a semi-transparent green
893 box. Sequences aligned: *Vibrio alginolyticus VaPomAB*; *Vibrio mimicus VmPomAB*; *Shewanella*
894 *oneidensis SoPomA and SoPomB*; *Bacillus pseudofirmus BpMotPS*; *Bacillus subtilis BsMotPS*,
895 *BsMotAB*; *Bacillus alcalophilus BaMotPS*; *Escherichia coli EcMotAB*; *Salmonella enterica*
896 *SeMotAB*; *Campylobacter jejuni CjMotAB*; *Clostridium sporogenes CsMotAB*.

897

898 **Fig. S2 Cryo-EM of *VaPomAB* in LMNG detergent.**

899 **a**, A representative SEC profile of LMNG detergent purified *VaPomAB* complex. The fraction
900 used for preparing cryo-EM grids is indicated with a pink rectangular bar. **b**, SDS gel from **a** is
901 shown. **c-d**, Flowchart of the data processing of *VaPomAB* in LMNG in cryoSPARC that results
902 in the final cryo-EM structure of *VaPomAB* at around 2.5 Å resolution after non-uniform
903 refinement. **e**, Gold standard (0.143) Fourier shell correlation (GSFSC) curves for *VaPomAB* in
904 LMNG. **f**, Particle directional distribution of *VaPomAB* in LMNG. **g**, Cryo-EM density map of
905 *VaPomAB* in LMNG detergent colored by local resolution (in Å) estimated in cryoSPARC. **h**,
906 Representative model segments fitted into EM density.

907

908 **Fig. S3 Cryo-EM of *VaPomAB* in MSP1D1 lipid nanodisc.**

909 **a**, SDS gel analysis of purified *VaPomAB* in MSP1D1 lipid nanodisc. **b**, Flowchart of the data
910 processing of *VaPomAB* in MSP1D1 lipid nanodisc in cryoSPARC that results in the final cryo-
911 EM structure. **c**, The final cryo-EM map of *VaPomAB* in MSP1D1 lipid nanodisc at around 3.9 Å
912 resolution. **d**, Cryo-EM density map of *VaPomAB* in MSP1D1 lipid nanodisc colored by local
913 resolution (in Å) estimated in cryoSPARC. **e**, Gold standard (0.143) Fourier shell correlation
914 (GSFSC) curves for *VaPomAB* in MSP1D1 lipid nanodisc. **f**, Particle directional distribution of
915 *VaPomAB* in MSP1D1nanodisc. **g**, Representative model segments fitted into EM density.

916

917 **Fig. S4 Cryo-EM of full length *VaPomAB* in saposin lipid nanodisc.**

918 **a**, SDS gel analysis of the purified full length *VaPomAB* in saposin lipid nanodisc. **b-c**, Flowchart
919 of the data processing of full length *VaPomAB* in saposin lipid nanodisc in cryoSPARC that results
920 in the final cryo-EM structure. **d**, The final cryo-EM map of *VaPomAB* in saposin lipid nanodisc
921 at around 6.3 Å resolution after local refinement. **e**, Gold standard (0.143) Fourier shell correlation
922 (GSFSC) curves for *VaPomAB* in saposin lipid nanodisc. **f**, Particle directional distribution. **g**,
923 Cryo-EM density map of *VaPomAB* in saposin lipid nanodisc colored by local resolution (in Å)
924 estimated in cryoSPARC.

925

926 **Fig. S5 Dynamics of *VaPomA* PI and TM1 helices.**

927 **a-c**, Representation of the *VaPomAB* LMNG unsharpened electrostatic potential maps at low
928 threshold showing the conformational dynamic of PI helices that interact with PomB plug motifs,
929 and the flexibility of the corresponding TM1 helices. **d-f**, Representation of the *VaPomAB*
930 MSP1D1 lipid nanodisc unsharpened electrostatic potential maps at low threshold. **g-i**,
931 Representation of the full length *VaPomAB* saposin lipid nanodisc unsharpened electrostatic
932 potential maps at low threshold.

933

934 **Fig. S6 Na⁺ translocation pathway and dynamics of PomB D24.**

935 **a-b**, The trajectories of the side chain dynamics of D24 in PomB chain 1 and 2 obtained from two
936 independent MD simulations. **c**, The cryo-EM Na⁺ binding sites. The modelled Na⁺ ions are shown
937 by blue spheres. **d**, The Na⁺ binding sites captured in MD simulations. The average density of Na⁺
938 ions is represented by red mesh in **c** and **d**.

939

940 **Fig. S7 Hydration of T33 and the Na⁺ translocation pathway and side chain dynamics of**
941 **T158, T185 and T186 obtained from explicit solvent MD simulations.**

942 **a-b**, The hydration and Na⁺ binding in the engaged and disengaged state, respectively. The average
943 density of water molecules is represented by mesh in green. **c**, A snapshot from the MD simulations
944 to show the hydration of T33 in PomA chain 5. **d-f**, The MD trajectories of the side chain dynamics
945 of T186, T185 and T158 in PomA chain 2 and 5.

946

947 **Fig. S8 densities of ion selectivity cavities.**

948 **a**, View from the plane of the membrane, showing the position of ion selectivity cavity within the
949 complex. **b-f**, ion selectivity cavities from PomA chains 1 to 5. EM densities are overlaid on the

950 corresponding local regions. **g-i**, L36 from PomB chain 1 and chain 2 interaction environments,
951 showing that PomB chain 1 L36 interacts PomB chain 2 F47.

952

953 **Fig. S9 Conservation (calculated with ConSurf) analysis of VaPomA and VaPomB.**

954 **a-b**, Conservation (calculated with ConSurf) of the surface residues of VaPomA from external and
955 internal sides; C α atom representation (shown as spheres) of the model colored by conservation.
956 **c**, Conservation of the residues of the Na⁺ ion selectivity filter and permeation pathway from the
957 periplasmic side, both external and internal views are shown. **d**, Conservation of the residues of
958 PomA cytoplasmic domain, highlighting the locations of the positively charged residues from the
959 principal face involved in FliG torque helix binding. **e**, Same as in **d**, but highlighting negatively
960 charged residues from the complementary face. **f**, Conservation of the surface residues of VaPomB,
961 highlighting the strictly conserved residues. **g**, Same as in **f**, but rotated 180 degrees.

962

963 **Fig. S10 Conformational isomers of VaPomAB M155.**

964 **a**, View from the plane of the membrane, showing the position of PomA M155 within the complex.
965 **b-f**, M155 isomers from PomA chains 1 to 5. EM densities are overlaid on the side chains of M155.
966 **g**, Conformational isomers of M155 viewed from the top of the membrane.

967

968 **Fig. S11 5:2 rotary motor directional rotation ‘reinforcement’ point.**

969 **a**, Proton-driven flagellar stator unit CjMotAB (PDB: 6YKM). **b**, Conformational isomers of L158
970 near MotB engaged D24 and disengaged D24. **c**, Conformational isomers of L158 viewed from
971 the top of the membrane. Solid circle indicates the rotational direction of MotA around MotB. The
972 potential clash that would occur if PomA rotated CCW around PomB is indicated with a red
973 heptagon. **d**, Proton-driven Ton ExbB-ExbD complex (PDB: 6TKI). **e**, Conformational isomers of
974 L145 near ExbD engaged D25 and disengaged D25. **f**, Conformational isomers of ExbB L145
975 viewed from the top of the membrane. Solid circle indicates the rotational direction of ExbB
976 around ExbD. The potential clash that would occur if ExbB rotated CCW around ExbD is indicated
977 with a red heptagon.

978

979 **Fig. S12 VaPomAB model B-factor distribution.**

980 Top (**a**) and side views (**b**) of the PomAB model (LMNG dataset) colored by B-factor distribution
981 (atomic displacement factor).

982

983 **Fig. S13 H⁺- and Na⁺- driven stator units PomB/MotB plug motifs organization.**

984 **a**, Side view of the proton-driven stator unit *CjMotAB* in its auto-inhibited state. **b**, *CjMotAB*
985 viewed from the top of the membrane. **c**, Side view of the sodium-driven stator *VaPomAB* in its
986 auto-inhibited state. **d**, *VaPomAB* viewed from the top of the membrane. Rotational direction of
987 the stator unit is indicated. **e**, The unique trans mode organization of the plug motifs tightly blocks
988 the CW rotation of the stator unit.

989

990 **Fig. S14 Mutational analysis for *VaPomA* and *VaPomB* plotted onto the *VaPomAB* structure.**

991 **a-b**, The motility phenotypes of *VaPotAB* *PomA* (**a**) and *PotB* (**b**) point mutants were analyzed
992 using soft-agar motility plates containing 0.2% agar. **c-d**, Swimming efficiency of the *VaPotAB*
993 point mutants, showing the mutated residues as $C\alpha$ spheres on the *PomA* (purple) and *PomB* (white)
994 structure.

995

996 **Fig. S15 Conformational changes of *PomA* cytoplasmic domain during stator unit activation**
997 **and disassembly from the rotor.**

998 **a**, *PomA* cytoplasmic domain is asymmetric, and one site of the CH-CI detachment is indicated in
999 dashed line. Inactive stator unit orients its cytoplasmic domain towards the rotor to contact FliG
1000 torque helix through FliG torque helix ‘matching sites’ ((1)-(2)). During the activation, all five
1001 CH-CI interactions established, and *PomA* cytoplasmic domain becomes symmetric ((3)-(4)). The
1002 rotor could rotate either CW or CCW direction, depending on how it interacts with the stator unit.
1003 Stator unit disassembly from the rotor when external torque is decreased ((5)-(6)). **b**, In this model,
1004 during the stator unit activation, *PomA* cytoplasmic domain remains asymmetric ((3)-(4)); one site
1005 of the CI helix attaches to the PI helix and the adjacent CI helix detaches from the PI helix,
1006 sequentially creating a FliG torque helix ‘catching’ site that interacts with the FliG torque helix.